The mineralogy of weathering products of Bi-bearing tennantite – clues for the process and the mobilisation of heavy metals and toxic elements

Keim, M.; Staude, S.; Marquardt, K.; Bachmann, K.; Opitz, J.; Markl, G.;

Originally published:

November 2018

Chemical Geology 499(2018), 1-25

DOI: https://doi.org/10.1016/j.chemgeo.2018.07.032

Perma-Link to Publication Repository of HZDR:

https://www.hzdr.de/publications/Publ-27267

Weathering of Bi-bearing tennantite

Maximilian F. Keim[1], Sebastian Staude[1*], Katharina Marquardt[2], Kai Bachmann[3], Joachim Opitz[4], Gregor Markl[1]

[1] Department of Geosciences, University of Tübingen, Wilhelmstraße 56, 72074 Tübingen, Germany

[2] Bayerisches Geoinstitut, University of Bayreuth, 95440 Bayreuth, Germany

[3] Helmholtz-Institut Freiberg für Ressourcentechnologie, Chemnitzer Straße 40, 09599 Freiberg, Germany

[4] Department of Mineralogy, University of Stuttgart, Azenbergstraße 18, 70174 Stuttgart, Germany

*corresponding author: Sebastian Staude

mail: Sebastian.staude@uni-tuebingen.de

phone: +49 (0)7071-29-73080

Abstract

The complex sulfosalts of the tennantite-tetrahedrite solid-solution series [called fahlore; $(Cu,Ag)_6Cu_4(Fe,Zn,Cu,Hg,Cd)_2(Sb,As,Bi,Te)_4(S,Se)_{13}$] are widespread in many geological environments and since they incorporate heavy metal and toxic elements, a better understanding of their weathering process and the element mobility is important to evaluate environmental risks. In this study, the weathering of Bi-rich members of this mineral group were investigated using microscopy, EMPA, SEM, TEM, LA-ICP-MS, Raman, µXRD and MLA.

Observations reveal a succession of four distinct stages of weathering: During stage 1, irregular tubes within the fahlore show an assemblage of nm- to µm-sized roméite group minerals, tripuhyite, crystalline Cu-oxides, and crystalline Cu-sulfides, all of which crystallized from a gel-like phase. The textural appearance and the occurrence of these secondary sulfides indicates a low redox-potential during this stage and a low fluid/rock ratio, typical of cementation zones. Mass balance calculations show that during this stage all Zn and the majority of As and S are released to the weathering fluids, whereas Cu and Si are added externally. Bismuth is immobile in this stage and Sb and Fe are immobile, if Bi is sufficiently available from fahlore, but both are partly released into the fluid, if the fahlore did not contain sufficient Bi. During stage 2, amorphous and nano-crystalline arsenates replace fahlore as weathering fronts. Such assemblages indicate a higher redox-potential than in stage 1, typical for oxidation zones. Mass balance calculations reveal that Zn, Sb, and S and partially Cu are lost, whereas Fe and Ba are added during this stage. Arsenic and Bi are immobile. Stage 3 occurs only locally, dissolving former weathering stages and/or precipitating amorphous Cu-arsenates and Cu-silicates, respectively, and reflects processes in micro-compartments, not characteristic for the general weathering process. Stage 4 is characterized by the formation of crystalline Bi-, Cu-, Ba-, Ca- or Al-bearing arsenates and Cu-carbonates mostly along cracks, spatially independent of the precursor fahlore. Copper and As originate from older weathering assemblages, whereas many other elements are derived externally (Ca, Ba, Al). This stage reflects the increasing importance of the local host rock and gangue mineralogy, as it is typical in near surface environments of oxidation zones or on mine dumps, where elements are highly mobile and a high fluid/rock ratio prevails (gossan mineralization).

The temporal evolution of fahlore weathering textures reflects the transition from fresh ore to cementation zone, oxidation zone and finally gossan textures and assemblages in one hand specimen. Thus, one fahlore grain can record the uplift and erosion and the increasing fluid/rock interaction of a weathered ore deposit with time. Tube-like textures similar to the ones observed in the stage 1 have been reported from other weathering environments and from a variety of element, oxide, arsenide, and sulfide phases. They also were produced during experimental reaction of

ilmenite with HCl-bearing fluids. This is clear evidence, that the diffusive process during the first contact with alteration fluids to form cementation zone assemblages is a basic physical process and that it is not only valid for fahlore.

Keywords

Tennantite-tetrahedrite, fahlore, weathering, bismuth, element mobility, cementation zone, oxidation zone, Schwarzwald

1. Introduction

Minerals of the tennantite-tetrahedrite solid-solution series (in the following referred to as fahlore) have the general formula of $(Cu,Ag)_6Cu_4(Fe,Zn,Cu,Hg,Cd)_2(Sb,As,Bi,Te)_4(S,Se)_{13}$ (Johnson et al., 1986; Breskova and Tarkian 1994; Makovicky, 2006 and references therein; Moëlo et al., 2008). Between the common As- and Sb-endmembers, a complete solid-solution is known (Johnson et al., 1986). Bismuth-rich varieties of fahlore, however, are rare in nature (Johnson et al., 1986) and up to date, no endmember has been found in nature or has been synthesized (Gołębiowska et al., 2012). Maximum reported Bi contents for fahlore are up to 22 wt.% from the Wittichen area in the Schwarzwald ore district, Germany (Staude et al., 2010; George et al., 2017).

Fahlore was and is economically important, as it is one of the most widespread silver-bearing ore minerals (Wu and Petersen 1977). It is the most common sulfosalt (Wu and Petersen 1977) occurring in a wide variety of geological settings, mostly in hydrothermal veins, but also in regional metamorphic, skarn, SEDEX, VMS, MVT, black shale and orogenic gold deposits, as well as in porphyry and active black smoker systems (e.g., Leach et al., 1988; Vavelidis and Melfos 2004; Staude et al., 2010; Mueller and Muhling, 2013; Kozub, 2014; Plotinskaya et al., 2015; Repstock et al., 2015; Wohlgemuth-Ueberwasser et al., 2015; George et al., 2017). Therefore, fahlore found its way to relatively small mine dumps from the Bronze Age (e.g., Ixer, 2001) to today's giant mine and tailings dumps of these various types of deposits.

Under oxidizing, near surface conditions, fahlore is not stable anymore. As a consequence, it undergoes dissolution and/or thermodynamically more stable secondary phases form (e.g., Arroyo and Siebe 2007; Roper et al., 2012; Keim and Markl 2015; Borčinová Radková et al., 2017). During this process, heavy metals and toxic elements are commonly released to the environment (e.g., Reich and Vasconcelos 2015). Which secondary phases form and, hence, which components are released to the environment, depends on the composition of the primary mineral and the physiochemical conditions of the weathering fluids (e.g., Keim and Markl 2015; Lara et al., 2016; Keim et al., 2017).

The wide range of toxic elements like Sb, As, Cu, Hg, and Cd (Prasad, 2013) incorporated in fahlore makes a further understanding of fahlore weathering crucial to identify their behaviour in near-surface environments. Given their widespread occurrence, and the environmental risks linked to their weathering, studies on the weathering behaviour of fahlores are surprisingly scarce. Nickel et al. (2007) investigated the secondary mineral assemblage of tennantite from Bali Lo (Australia) which weathered in the presence of a Pb-rich fluid to form euhedral Cu- and Pb-bearing arsenates in voids (boxwork) of the dissolved fahlore. Weathering of tennantite and sphalerite from tailings material of a tungsten mine (Mt. Pleasant, Canada) was investigated by Petrunic et al. (2009). They found that a nano-crystalline or amorphous Fe-Zn-As-oxidic phase formed together with Cu-sulfides. They also concluded that the chemistry of nano-scale phases is inconsistent with saturation indices based on

pore-water analyses and therefore suggested, that the formation of these phases may not be thermodynamically controlled. Only recently, the weathering chemistry and mineralogy of Sb-dominated fahlore was investigated by Borčinová Radková et al. (2017) focusing on the mobility of the potentially toxic elements As, Sb and Cu during the weathering process, but not on the process itself. They found, that these elements show different mobility during weathering. Copper and arsenic are generally retained by mostly X-ray amorphous phases, while antimony is only partially bound by triphuyite and roméite. Zinc and S are generally lost during weathering of fahlore. Arsenic-dominated fahlore forms an X-ray amorphous weathering phase with Cu, As and Fe (Borčinová Radková et al., 2017). The investigation by Borčinová Radková et al. (2017) deals with a certain geological environment (e.g., fahlore composition, chemistry, pH, and fO_2 of weathering fluid) specific to the weathering of the specific, investigated deposit (hydrothermal quartz-siderite-sulfide vein-type deposits at Špania Dolina-Piesky and L'ubietová-Svätodušná, Central Slovakia). In order to understand the common processes active during fahlore weathering in general, and the differences of the processes related to various geochemical environments, it is important to broaden the observation base.

In this contribution, we present the first study of Bi-bearing (up to 15.9 wt.% Bi) and As-dominated fahlore (with variable As/Sb ratios) exposed to long-term weathering from different geological environments in the Schwarzwald (SW Germany) using scanning electron (SEM) and light microscopy, electron-microprobe (EMP), Raman, micro X-ray diffraction (μXRD), laser-ablation inductively-coupled plasma mass spectrometry (LA-ICP-MS), mineral liberation analyses (MLA), and transmission electron microscopy (TEM) in order to evaluate the general weathering processes and the mobility of elements.

2. Geological background

The northern Schwarzwald hydrothermal veins are partly hosted by Variscan basement rocks (granites and metasedimentary gneisses), but mostly by Permian to Lower Triassic clastic redbed sediments (Geyer and Gwinner, 2011; Villinger and Zedler, 2006; Rupf and Nitsch, 2008) which were unconformably deposited on the basement. The multi-element veins at Wittichen are situated in the granitic basement directly underneath the unconformity, whereas the other investigated deposits (Neubulach, Freudenstadt, Königswart) are hosted by the Lower Triassic sediments. Middle Triassic shale and carbonate rocks are partly preserved in some areas, but are mostly eroded due to the Schwarzwald uplift during the Paleogene-Neogene Upper Rhine Graben formation (Geyer and Gwinner, 2011). The veins do not cut these Middle Triassic rocks, but in the vicinity of the veins of Neubulach, <5 m of Middle Triassic limestone is still preserved on ridges next to the veins (Metz,

1977; Göb et al., 2015). More information on the investigated veins and their geology can be found in Metz (1977); Werner and Dennert (2004); Werner (2012); Staude et al. (2010, 2011, 2012a, b); Markl et al. (2014a); Markl (2015, 2016); and Göb et al. (2015).

The primary hydrothermal veins were formed during post-Variscan extensional tectonics (Franzke and Werner, 1994; Pfaff et al., 2009; Staude et al., 2009) by mixing of an ascending metal- and Na-Ca-rich brine with a stagnating Na-dominated brine near the basement-cover unconformity (Bons et al., 2014; Burisch et al., 2016). About 100 of the Schwarzwald hydrothermal mineralizations were age-dated and reveal an intermittent activity since 310 Ma with peaks during Permian pull-apart basin formation, the Jurassic opening of the North Atlantic and the Paleogene-Neogene formation of the Upper Rhine Graben (Walter et al. in press; Pfaff et al., 2009 and references therein). The types of mineralization and their metal content vary with age and also with their spatial distribution within the Schwarzwald (Metz et al., 1957; Bliedtner and Martin, 1986; Staude et al., 2009; Walter et al., 2016). The area of investigation is dominated by quartz veins with variable amounts of barite and minor amounts of fluorite. Sulfide minerals are Bi-bearing As-dominated fahlore, chalcopyrite, pyrite, and locally large amounts of emplectite, wittichenite, native Bi, and various Cu-sulfides (Staude et al., 2010, 2012a). Formation temperatures for these veins as recorded by fluid inclusions range from 50°C to 150°C reflecting the varying proportions of fluids involved in mixing (Staude et al., 2012a; Walter et al., 2018).

2.1. Weathering of hydrothermal veins in the Schwarzwald

The secondary mineralization and its elemental redistribution processes in the Schwarzwald were investigated by Göb et al. (2011, 2013a); Burmann et al. (2013); Markl et al. (2014a, b); Haßler et al. (2014); Göb et al. (2015); Keim and Markl (2015); and Keim et al. (2016). They occurred since the uplift of the Schwarzwald in the Neogene and Quaternary (after 15 Ma, Hautmann and Lippolt, 2000). Available formation ages of the secondary phases from the investigated deposits are $^{40}Ar/^{39}Ar$ ages on secondary hollandite from Wittichen (1.0±0.1 Ma; Hautmann and Lippolt, 2000) and a U-Pb isochron age on secondary calcite from Wittichen (5.2±0.3 Ma; Staude et al., 2012b). Other ages from Schwarzwald supergene weathering minerals are 1.7±0.4 Ma (Pfaff et al., 2009) and 0.3±0.04 (Hofmann and Eikenberg, 1991) for supergene uranium phosphates, and eight ages between 10.1±0.3 and 0.84±0.03 Ma on botryoidal goethite (Lippolt et al., 1998). 64 hydrothermal and supergene carbonates have been dated by Walter et al. (in press) between 40.0±11 Ma and 0.6±0.19 Ma, however, it is in most cases not possible to discriminate between hydrothermal and supergene carbonates. Supergene minerals formed in various settings:

- in the oxidation zone of the veins (Markl et al., 2014a, b) during natural and mining processes (e.g., concrete in the Clara mine and fire-setting; Kolitsch, 2000; Keim et al., 2017)
- after the mining within the abandoned mines (e.g., pyromorphite, arsenates and sinters in mines, (Burmann et al., 2013; Markl et al., 2014a, b; Göb et al., 2015) or
- on waste dumps (Markl et al., 2014a; Keim et al., 2017).

Primary minerals of the investigated mines were exploited for Ag, Co (Wittichen area only) and Cu and additionally for azurite as pigment in Neubulach (Werner and Dennert, 2004). Mining occurred mainly in the 13th (Neubulach) and 17th to 19th century (Werner and Dennert, 2004; Markl, 2005), exposing large parts of the dumps to weathering for several centuries.

The geochemistry of water responsible for weathering of primary mineralization and precipitation of secondary minerals were investigated by Zhu et al. (2003); Bucher et al. (2009); Göb et al. (2013b, 2015); and Markl et al. (2014a) using recent mine waters, partly directly taken in the vicinity of newly formed arsenates and sinters inside the Wittichen mines. The investigated water was influenced by seasonal changes (amount of rain, melting of snow; Göb et al., 2015), organic material (organic phosphate to form pyromorphite, Burmann et al. (2013), farming (fertilizers; Göb et al., 2015 and references therein), or other human activity (salt on roads in winter; Göb et al., 2015). In Neubulach, Göb et al. (2015) showed that water dripping from sinters is more influenced by fluid-rock interaction than water flowing on the mine floor, and that the sinter-forming water dissolved azurite and precipitated malachite.

2.3. Sample description

Samples were collected from the northern part of the Schwarzwald ore district (SW Germany) where fahlore-bearing hydrothermal quartz-barite (±fluorite) veins (Staude et al., 2010) are exposed to weathering. Samples were collected from the mining areas of Neubulach, Königswart, Freudenstadt and Wittichen/Reinerzau (Alte Gabe Gottes mine and Schmiedestollen dump; electronic supplementary material (ESM) Figs. 1 and 2, see Markl, 2015 and 2016 for detailed descriptions of these localities). The sample suite covers Bi-bearing fahlore as the main sulfide mineral (Neubulach and Freudenstadt veins, Alte Gabe Gottes mine, Reinerzau), Bi-bearing fahlore together with large quantities of emplectite (Königswart veins), and Bi-bearing fahlore together with large amounts of emplectite, native Bi, wittichenite, other Cu-dominated minerals, Co-Ni arsenides, and frequently hematite in the gangue (Schmiedestollen dump, Wittichen). Generally, fahlore in the investigated deposits is often overgrown by euhedral quartz and barite and only rarely shows euhedral surfaces. Chalcopyrite and pyrite are present in most samples in small quantities and they are overgrown by

fahlore. The carbonate synchysite-(Ce) frequently forms small euhedral crystals together with hematite, both enclosed by quartz in the sample from the Alte Gabe Gottes mine, whereas other primary carbonates were not observed in other samples.

3. Analytical Methods

EMPA, SEM, Raman spectroscopy, and µXRD were performed at the University of Tübingen, Germany, LA-ICP-MS at the University of Stuttgart, Germany, TEM at the Bayerisches Geoinstitut Bayreuth, Germany, and MLA at the Geometallurgy Laboratory of the Helmholtz Institute Freiberg, Germany.

3.1. EMPA, SEM

For qualitative and quantitative determination of the major and minor element compositions of the fahlores and weathering products, a JEOL 8900 electron microprobe was used. Analyses were carried out in wavelength-dispersive (WD) mode using an acceleration voltage of 25 kV (sulfides) or 20 kV (secondary phases) and a probe current of 20 nA. For the sulfides, a focused beam and for the weathering products a 2-5 µm probe diameter was used. The peak overlap of As and Sb was corrected by a factor of 0.0128, of S and Co by 0.0003, of Pb and Bi by 0.0209, and of Ce and Ba by 0.0630. The elements for the quantitative program were selected after qualitative analyses using energy dispersive X-ray spectroscopy (EDS) mode. Details of the used WD-configuration, including standards, counting times of the peak/background, analyzed fluorescence lines and the average detection limits are presented in Table 1 and 2 in the ESM. Visual images and qualitative EDS spectra were obtained using a TM3030+ Tabletop microscope from Hitachi. To avoid the peak overlap of the S Kα- with the Bi Mα-lines for the elemental maps, the Bi Mβ-line was used instead.

3.2. µXRD analysis

µXRD was used to characterize the weathering products of fahlore using a Bruker D8 Discover GADDS Θ/Θ micro-diffractometer. A Co anode (wavelength λ = 1.79 Å) at 30 kV, 30 mA, and room temperature was used. A mono-capillary with a 50 µm pinhole was used together with a VÅNTEC500 detector (Berthold et al., 2009). The patterns were integrated individually for each sample using a step size of 0.05 °2Θ. The incident angle of the beam was fixed to 15° and measurement time was set to 120 s per frame. Representative XRD patterns are shown in the ESM Fig. 3.

3.3. Raman

Raman analyses were performed to identify the fahlore weathering phases. A confocal Renishaw InVia Reflex Raman spectrometer with a laser wavelength of 532 nm and WiRE 3.0 software was used. The spectra were compared to reference spectra of the RRUFFTM database (Downs, 2006). Representative Raman spectra are shown in the ESM Fig. 4.

3.4. TEM

TEM was performed using a FEI TitanG2 80-200 at 200 kV acceleration combining diffraction methods with spectroscopy and imaging. Chemical composition was determined by EDS using the ChemiSTEM technology with four SDDs (XFlash 5030 detector) symmetrically mounted in the TEM column around the optical axis. Each SDD has an active area of 30 mm^2, adding up to an overall detector area of 120 mm^2 covering a solid angle of 0.9 sr. The element distribution maps were acquired in scanning transmission electron microscopy mode (STEM). At each pixel of the map a full energy dispersive X-ray spectrum was acquired. In order to obtain a high image resolution, the smallest condenser lens (C2) aperture of 50 µm was used while having a count rate of about 2000 counts per second by operation at relatively high electron currents of about 0.2 nA. The dwell time was set to 3 µs. The overall measurement time for the elemental STEM-EDX mapping was about 4 hours.

3.5. LA-ICP-MS

Elemental concentrations in minerals were determined by ICP-MS analyses with an AGILENT 7700 spectrometer after laser ablation with a CETAC LSX-213 laser system. In a first series of measurements, the diameter of the ablated spots was 50 µm. The laser energy was set to 40% of the maximum (100% = 4 mJ at a spot diameter of 150 µm), at a laser pulse frequency of 10 Hz. In a second series, a spot diameter of 25 µm and a laser energy of 60% was used. A mixed helium and argon gas flow with 500 ml/min and 800 ml/min, respectively, served as carrier of the ablated material. Reference materials were DLH8 from P&H Developments Ltd., a NIST (National Institute of Standards and Technology, USA) 612 glass and sphalerite standard MULZnS-1 (Onuk et al., 2017). The validity of the calibration with the DLH and the NIST glass and reproducibility were checked with the reference materials Diorite (DRN) and Zinnwaldite (ZW-C) from Service d'Analyses des Roches et des Mineraux du CNRS. Lithium-borate glass disks of both were prepared using 0.6 g of powder of these reference materials and 3.6 g of lithium borate.

The data acquisition was performed using the Agilent Mass Hunter software (version B.01.01). Each analysis comprised the acquisition of the individual background ion intensities (gas-blank) for 20 s followed by the acquisition of the ion intensities on laser irradiation of the sample spot for 40 s. In the off-line data evaluation, the analytical signal of each ion was corrected by the subtraction of the corresponding averaged background intensity. Within a selected appropriate interval of the ablation time profile, after each mass cycle the corrected individual ion intensities were integrated and divided by the integrated corrected intensity of the selected isotope of the reference element. From these values, relative elemental concentrations were calculated from the abundance of the corresponding isotope assuming a natural isotopic distribution and an individual calibration factor which was determined under the same experimental conditions. The software used for calibration and data evaluation was developed by Massone et al. (2013) and Baggio et al. (2018).

The following isotopes were monitored: 31P, 51V, 52Cr, 55Mn, 59Co, 60Ni, 66Zn, 71Ga, 72Ge, 95Mo, 107Ag, 111Cd, 115In, 118Sn, 205Tl, 208Pb, 209Bi. This selection excludes isobaric interferences with isotopes of other elements. In the case where two isotopes were analyzed, very similar corresponding individual elemental concentrations were obtained, which shows the absence of significant matrix effects. For this reason, the given values are the average of the corresponding individual elemental concentrations. While running the analyses, signals of laser ablation were stable for all samples.

All elemental concentrations were calculated relative to the elemental concentrations of Bi (atelestite) and Cu (all other phases) as internal standard elements. The absolute elemental concentrations of both were previously measured with the EMP. The same spot target was applied for both EMP and LA-ICP-MS ablation.

MLA

The MLA system used comprises of an FEI Quanta 650F scanning electron microscope equipped with two Bruker Quantax X-Flash 5030 energy-dispersive X-ray spectrometers and the MLA software suite, version 3.1.4, for automated data acquisition. More detailed information about the functionality of the MLA system can be found in Fandrich et al. (2007), details about the data processing are shown in Bachmann et al. (2017). Consistent operating conditions were applied for all samples using the GXMAP measurement mode at 15 kV acceleration voltages, 6 nA probe current, 0.25 µm/pixel, 15 ms acquisition time and a step size of 8 pixel.

3.6. Analytical limitations

A successful analysis of the supergene weathering phases by EMPA is limited by the high porosity, the instability of the phases under the electron beam, and the unknown water and carbonate content especially in the amorphous phases, resulting in low totals for most of the EMP analyses. The small grain size of a few µm down to a few nm limits the quantitative determination of the minerals by EMP, since mixed mineral analyses including the surrounding phases are produced. Therefore, only phases large enough to be confidently analysed were investigated by EMP. The qualitative EDX analyses of the µm-nm sized minerals using TEM must be also handled with care, because an overlap of different mineral phases cannot be completely excluded. Moreover, some phases seem to dehydrate in the vacuum of the microprobe (e.g., bariopharmacosiderite $[Ba_{0.5}Fe^{3+}_4(AsO_4)_3(OH)_4{\cdot}5H_2O]$ and some amorphous Cu-arsenates) resulting in shrinking cracks and an unknown loss of volatiles (ESM Fig. 5). Raman and LA-ICP-MS measurements are both limited by the small grain size, the occasionally low thermal stability, and porosity of the analysed phases. The µXRD measurements in the thin sections are limited by the intergrowth of many phases (sometimes with preferred orientation) within a single measurement spot, which induces overlaps of mineral reflexes. Moreover, the nm-sized crystals in the amorphous phases did not show distinctive reflexes, which is probably due to their small grain size.

4. Results

4.1. Identified phases

Besides optical identification of the large-grained primary sulfide minerals fahlore, chalcopyrite, emplectite, wittichenite, bornite, and Co-Ni-arsenides, the secondary weathering products were identified optically and by EMPA, SEM, TEM, µXRD, and Raman as explained above.

Secondary sulfides are covellite [CuS], spionkopite $[Cu_{39}S_{28}]$, chalcocite $[Cu_2S]$, acanthite $[Ag_2S]$, and cinnabar [HgS) based on EMPA, TEM-EDX, and Raman. In all cases, a unique identification by µXRD of these sulfides was not possible due to the small grain size or intergrowth with amorphous phases.

A fine-grained Cu-oxide phase was found with an average chemical formula of $Cu_{0.9}O$ (normalised to 1 atom per formula unit (apfu) oxygen; analyzed by TEM-EDX). A unique identification as tenorite [CuO] by electron diffraction was not successful, and hence, the phase will be named Cu-oxide phase in the following.

Frequently, Sb-Fe, Sb-Bi-Fe, and Bi-Fe oxide phases were found. The Sb-Fe phase was qualitatively analysed by EDX mapping and is interpreted to be tripuhyite $[Fe^{3+}Sb^{5+}O_4]$ or hydroxyferroroméite $[(Fe^{2+}_{1.5}\square_{0.5})Sb^{5+}_2O_6(OH)]$, but based on these analyses, it was not possible to distinguish between

them. In similar weathering environments, the occurrence of these phases has also been reported (Borčinová Radková et al., 2017; Mills et al., 2017). The Sb-Bi-Fe phase was studied by TEM. EDX mapping gives an average chemical formula of $Cu_{1.0}Sb_{1.1}Bi_{1.0}As_{0.3}Fe_{0.7}O_{7.8}$ (normalized to 1 apfu Bi; see Table 1). There is no known mineral with that composition, however, it is similar to members of the cubic roméite group. The elongated crystal morphology, however, seems to fit better to members of the tetragonal phase tripuhyite. In two electron diffraction patterns from different locations in a sample from Neubulach, d-spacings were measured and are listed in ESM Table 3. Unfortunately, the relative positions of the diffraction spots of the diffraction patterns do neither prove a cubic nor a tetragonal symmetry, even in connection with the measured angles in ESM Fig 6. The measured d-spacing, however, shows a good agreement with the d-spacings of roméite, as evident from ESM Table 3. Those d-spacings which are not in agreement with roméite have a reasonable fit with d-spacings of triphuyite, especially considering their nano-crystalline nature. Small crystallite sizes can result in delta d/d errors as large as 5% following the arguments of Biskupek and Kaiser (2004). A mixture of both phases (roméite group mineral and a triphuyite-like phase) is thus a reasonable assumption. While it seems likely that both phases can incorporate elevated amounts of Bi, the exact influence of Bi on the lattice parameters is unknown. In the following, the mixture of the tripuhyite-like phase and roméite will be named roméite group mineral (RGM) if used generally or Bi-Fe-bearing RGM, Bi-Sb-bearing RGM, or tripuhyite/hydroxiferroroméite if used for a specific chemistry. Interestingly, Walenta (1983) described from Neubulach the occurrence of an Sb-Bi-Fe-phase called "bismutostibiconite" $[Fe^{3+}_{0.5}Bi^{3+}_{1.3}Sb^{5+}_{1.7}O_7]$, the IMA status of which as a mineral, however, was discredited (Atencio et al., 2010; Christy and Atencio, 2013). It is likely, that the mineral analysed by Walenta (1983) is the RGM found during this study. The Bi-Fe-bearing RGM was identified by EDX mapping and could represent another yet unknown member of the RGM, but was not further investigated.

Frequently, a Cu-As phase was found, which is characterized by either no crystallinity or nm-sized crystal aggregates in an amorphous ground mass. Raman measurements show that As is present as arsenate with some evidence of H_2O (ESM Fig 4). Other identified phases are amorphous and botryoidal Cu-Silicates, amorphous red Fe-Cu-oxides, and amorphous Bi-carbonates.

The well-crystallized arsenates mixite $[BiCu_6(AsO_4)_3(OH)_6{\cdot}3H_2O]$, olivenite $[Cu_2AsO_4(OH)]$, zálesiite $[CaCu_6(AsO_4)_2(AsO_3OH))OH)_6{\cdot}3H_2O]$, tangdanite $[Ca_2Cu_9(AsO_4)_4(SO_4)_{0.5}(OH)_9{\cdot}9H_2O]$, dussertite-arsenogoreceixite $[BaFe_3^{3+}(AsO_4)(AsO_3OH)(OH)_6$; $BaAl_3(AsO_4)(AsO_3OH)(OH)_6]$, and bariopharmacosiderite were identified by Raman, µXRD and EMPA (Table 4 ; ESM Figs. 3 and 4) as were the Cu-carbonate minerals malachite and azurite.

4.2. Weathering stages of fahlore

Based on textural evidence, the weathering of fahlore can be subdivided into four weathering stages (Stage 1-4), which are distinguished by textural appearance and phase assemblages. Each weathering stage is developed in variable amounts in the samples and sometimes, one or the other is lacking.

4.2.1. Stage 1 weathering

This stage occurs in most of the investigated fahlore samples and is characterized by the replacement of fahlore by Cu-sulfides, the Cu-oxide phase, and the RGM-tripuhyite-like phase intergrowth (Figs. 1-4). The Cu-sulfides covellite, spionkopite, and chalcocite commonly occur within the same sample (Fig. 2). Additional Cu-sulfides may be present. Within the Cu-oxide phase, rare nm-sized acanthite or cinnabar grains were observed.

In most cases, fahlore is replaced by the secondary assemblage in an irregular network of 30-100 µm thick veinlets and only rarely as a front from outside. These veinlets appear as finger-like tubes without a preferred orientation. They terminate in spherical shape, mostly without evidence of a previous crack in the fahlore (Fig. 1). In general, the finger-like tubes are made up by three different zones, consisting all of RGM and Cu-sulfides in a Cu-oxide groundmass. From the fahlore contact to the centre of the tubes, these zones are:

- Zone (1) shows layers, which are defined by alternating porosity and small grained (nm-sized) crystal phases.
- Zone (2) has no porosity, no layering and shows larger grains (several hundred nm to about 5 µm), crystals are arranged perpendicular to the tube.
- Zone (3) in the centre of the tube, forming a central pipe, has crystals arranged parallel to the tube, and sometimes hosts subhedral quartz surrounded by the RGM.

The grain size of zones (2) and (3) can show variations between samples, but the overall arrangement of the zones are similar at investigated localities.

Depending on the host fahlore chemistry, three different types of RGM phases form (assemblage 1.1: Bi-Sb RGM; assemblage 1.2: Sb-Fe RGM (hydroxyferroroméite); and assemblage 1.3: Bi-Fe RGM). If the fahlore is zoned, assemblage 1.1 to 1.3 can occur within a single fahlore grain (and can change within a single tube; see Figs. 1 and 4), but if the fahlore is homogeneous, only one of the assemblages occurs.

If chalcopyrite is intergrown with fahlore, nothing changes with respect to fahlore weathering stage 1. Some of the veinlets stop at the contact to chalcopyrite, some continue into it, in which case, the veinlets consist of a red homogeneous amorphous Fe-Cu-oxide phase.

Weathered native Bi (which occurs as associated mineral in the fahlore-bearing samples) shows similar finger-like tubes, which are, however, composed of an amorphous Bi-carbonate (Fig. 5). Intergrown aggregates of wittichenite and emplectite in the vicinity of fahlore from Neubulach exhibit the same finger-like textures as observed in fahlore (Fig. 5c). The contact of the tube to wittichenite or emplectite is porous and contains nm-sized Cu-sulfides. Towards the centre of the tube, the groundmass consists of a Bi-carbonate which includes µm-sized Cu-sulfides. The central pipe is composed of aggregates of the Bi-Sb-bearing RGM. Other minerals, in which the finger-like tubes were observed, comprise pyrite, gersdorffite, and nickeline, but it was not the topic of the present research to investigate these further.

4.2.2. Stage 2 weathering

This stage is dominated by an amorphous arsenate phase replacing fahlore (Figs. 6-8). In some cases, the stage 1 assemblage is unaffected by younger weathering, but it has also been observed that the Cu-oxides are partially replaced by Cu arsenates, independent of the sample locality. No textural or chemical differences between localities and their different fahlore compositions are observed. Partly, the weathering occurs in poorly developed finger-like textures, but the most common form are arsenate fronts replacing fahlore. The Cu-arsenate phase is texturally highly inhomogeneous: elongate and often curved areas with low porosity alternate with high porosity areas. This porosity is visible on a µm- and nm-scale. Some amorphous layers also show an increased amount of 2-10 nm large crystals of a Cu-oxide phase of unknown composition, whereas other amorphous layers are free of nano-crystals. Often, µm-sized euhedral barite crystals are intergrown or occasionally form alternating layers with the amorphous arsenate (Fig. 9a). Occasionally, small grains of acanthite or cinnabar were observed enclosed by the amorphous Cu-arsenates (Fig. 8). In one sample from Freudenstadt, also bariopharmacosiderite overgrown by barite and the amorphous Cu-arsenate was identified. In this sample, also illite is intergrown with the arsenate. Where chalcopyrite is intergrown with fahlore, an amorphous green arsenate replaces chalcopyrite. Native Bi is frequently surrounded by bismite, partly displaying a zonation (Fig. 5b).

4.2.3. Stage 3 weathering

This stage includes weathering steps postdating stage 2, but predating stage 4 weathering textures. Stage 3 weathering textures are specific for a certain sample location and, hence, not part of a general weathering process occurring in the same way at each locality.

In Neubulach, weathering stage 3 is characterized by a partial dissolution of stage 1 phases, affecting the Cu-sulfides and Cu-oxide phase, but not the RGM (Fig. 9). The dissolved areas are partly replaced

by an amorphous Cu-arsenate-sulfate phase which hosts abundant nm-sized Cu-bearing crystals of unknown composition. This replacement is only observed directly on the unaltered stage 1 assemblages (within 100-200 µm), whereas other affected areas leave behind the RGM only, which appears yellow-brown in transmitted light (Fig. 9).

In a sample from Königswart, amorphous Cu-silicates cement brecciated clasts of fahlore and weathering assemblage 2 (Fig. 10). The clasts are overgrown by botryoidal aggregates of an amorphous Cu-silicate I, followed by homogeneous amorphous Cu-silicate II which also hosts euhedral quartz crystals.

4.2.4. Stage 4 weathering

Weathering stages 1 and 2 replace fahlore in situ. In contrast, assemblages formed during stage 4 rarely replace minerals, but (partially) fill cracks or new fracture networks cutting through the primary hydrothermal minerals, the host rock, and older weathering assemblages of stages 1-3 (Fig. 11). The most frequent phases are azurite, malachite, and mixite. In one sample, azurite replaced Cu-arsenates of stage 2 (Fig. 11d). In this sample, azurite also infiltrates the stage 1 assemblage, excluding the RGM, but it is unclear whether it replaces it directly or fills the voids of weathering stage 3. No amorphous phases are present in this stage. Minerals identified are olivenite, dussertite-arsenogorceixite, tangdanite, zalesiite, mixite, bariopharmacosiderite, azurite, atelestite, and malachite which are partly accompanied by barite and quartz (the latter also formed during the same weathering process, not representing hydrothermal phases). The mineral assemblage varies from locality to locality (Table 4). Where malachite and azurite occur in the same sample, azurite typically forms in or close to fahlore, whereas malachite is the dominant mineral further away. In one sample, a quartz-hosted azurite vein cuts through hydrothermal gangue minerals and through fahlore-hosted, older weathering assemblages; at the contact with the latter, it changes to an unknown Ca-Cu-arsenate (Fig. 11c).

4.3. Mineral chemistry

4.3.1. Primary hydrothermal minerals

Detailed EMP analyses of fahlore from all localities can be found in Table 2. Samples of this study are all As-dominated showing molar X_{As} (As/(As+Sb)) between 0.6 and 1.0. The Bi content at each locality is variable, generally ranging between 1 and 12 wt.% (Fig. 12a). Maximum Bi-contents are 15.9 wt.% (Neubulach). Molar X_{Zn} (Zn/(Zn+Fe)) of the fahlores ranges widely between 0.0 and 0.9. The lowest Zn contents are found in Freudenstadt (median of 1.8 wt.%), followed by Königswart (median of 3.3

wt.%), Neubulach (median of 4.2 wt.%), and Wittichen (median of 5.8 wt.%) where also the highest variation is found (from detection limit to 7.9 wt.%). Silver contents reach up to 1.2 wt.%, Hg contents up to 0.9 wt.%, Co and Se contents up to 0.4 wt.%, respectively. Other trace elements identified by LA-ICP-MS are shown in Table 3. Most fahlore shows a growth and occasionally a sector zonation, but the observed weathering textures do not follow a certain chemical zone.

4.3.2. Secondary weathering phases – stage 1

Most of stage 1 weathering phases are too small for quantitative analyses by EMPA, however, chemical maps by SEM and TEM, and trace element analyses by LA-ICP-MS provide additional useful information on their composition and elemental distribution and allow to quantify phase compositions, although the attached error is admittedly large.

The matrix of stage 1 assemblage, the Cu-oxide phase, contains up to 3.1 wt.% As_2O_5, 1.2 wt.% Bi_2O_3, 1.6 wt.% SO_3 and other trace elements below 1 wt.% (Table 1).

Covellite, only analysed from Neubulach (TEM-EDX), is almost stoichiometric ($Cu_{0.99}S$; normalised to 2 apfu, average of 4 analyses) with Bi up to 5000 ppm as the main trace element (Table 2). Spionkopite was only analysed from Freudenstadt with Ag up to 1.2 wt.%, As up to 1.0 wt.%, and Bi up to 5400 ppm besides other trace elements (Table 2). The optically identified chalcocite shows an average chemical formula of $Cu_{2.5}S$ (normalized to 1 apfu S; TEM-EDX) and therefore too high Cu/S ratios.

Only the Bi-Sb RGM was analysed by TEM-EDX resulting in the formula $Cu_{1.0}Sb_{1.1}Bi_{1.0}As_{0.3}Fe_{0.7}O_{7.8}$ (normalized to 1 apfu Bi; see section 4.1). It contains traces of SiO_2, Al_2O_3, BaO, P_2O_5, and SO_3 (Table 1). A mixture of all stage 1 phases from Neubulach, analysed by LA-ICP-MS, resulted in up to 10 ppm V, 150 ppm Mn, 15 ppm Cr, 120 ppm Co, 10 ppm Ni, and 85 ppm Pb (Table 3, Fig. 13). Sample points where Cu-sulfides and the matrix were dissolved during stage 3, leaving voids and only the RGM behind, show higher Mn (up to 330 ppm) and Pb (up to 280 ppm) as well as lower Co (up to 6 ppm) and Ni (up to 2 ppm).

The amorphous red oxide phase in weathering stage 1 of chalcopyrite is dominated by Fe and Cu and was analysed from Wittichen and Königswart (n=10). Normalised to 100 mol%, the Fe content varies between 20.3 mol% and 33.6 mol%, the Cu contents between 7.7 mol% and 14.1 mol%. Other main components are variable and include As_2O_5 with up to 4.2 wt.%, SO_3 with up to 3.3 wt.%, and SiO_2 with up to 7.4 wt.%.

4.3.3. Secondary weathering phases – stage 2

The amorphous Cu-arsenates of stage 2 have variable amounts of Bi_2O_3 (up to 12.3 wt.%) and other components (Table 4). Some data of the Cu-arsenate phase are close to the stoichiometric composition of olivenite, however, the bulk of the data shows variable Cu/As ratios (Fig. 12c; Table 4). The totals of the EMPA range from 59 to 97 %, reflecting variable water content and a high and variable porosity.

Semi-quantitative TEM/EDX analyses were performed on the Bi-poor and Bi-rich zones of the amorphous Cu-arsenates (Fig. 7a, Table 1). The concentration of Bi_2O_3 is 3.7 and 9.1 wt.%, respectively, which is similar to the EMPA analyses (Table 4). The Bi-poor zone has lower As_2O_5 (17.0 wt.%) and CuO (28.5 wt.%) compared to the Bi-rich (27.5 wt.% As_2O_5 and 42.7 wt.% CuO) and higher SO_3 (28.6 wt.% compared to 3.5 wt.%). The Bi-poor zone also has higher Fe_2O_3 and SiO_2 (Table 4).

4.3.4. Secondary weathering phases – stage 3

The green amorphous to nano-crystalline arsenates of stage 3 (Fig. 9) are too small for identification by EMPA but were investigated by TEM. They contain 65.5 wt.% CuO, 13.0 wt.% As_2O_3, 10.0 wt.% SO_3, and 4.7 wt.% Bi_2O_3 (TEM-EDX) besides other trace elements presented in Table 1.

The two silicate-bearing phases from Königswart were analysed by EMPA. The botryoidal Cu-silicate has a higher silica content (22.6 wt.% SiO_2) and a higher total (89.3 %) compared to the homogeneous silicate (11.9 wt.% SiO_2, total: 73.6 %). The botryoidal phase also contains more As_2O_3 (6.4 compared to 5.1 wt.%), FeO (2.4 compared to 0.1 wt.%), and Bi_2O_3 (4.1 compared to 1.8 wt.%). Whether the lower total of the homogenous phase is due to a higher water or carbonate content, or due to porosity, remains unclear.

4.3.5. Secondary weathering phases – stage 4

The well-crystallized minerals of stage 4 are in most cases large enough for EMPA, however, a distinct identification was not always possible. Azurite was only analysed from Neubulach and contains up to 2.0 wt.% As_2O_5 and 1.1 wt.% FeO. Malachite was analysed from Neubulach, Freudenstadt, Königswart and Wittichen with ZnO up to 2800 ppm in Freudenstadt, Wittichen, and Neubulach, and up to 2.7 wt.% from Königswart. In analyses from Wittichen and Königswart, 3.8 and 0.14 wt.% Bi_2O_3 were detected, respectively. Other trace elements are not specific for a location and are As_2O_3 up to 2.9 wt.%, Sb_2O_5 up to 5300 ppm, and BaO up to 1400 ppm.

519 Mixite group minerals are abundant minerals of stage 4 from Königswart, Wittichen and Neubulach.
520 Wittichen samples show Ca-bearing mixite, samples from Neubulach and Königswart Bi-bearing
521 zalesiite (Table 4, see also Göb et al., 2011). All analysed mixite group minerals have SiO_2 up to 3.7
522 wt.%. Göb et al. (2011) also report rare earth elements from Neubulach with up to 1.07 wt.% Ce_2O_3.

523 All barite analyses of stage 4 contain Al_2O_3 (up to 9800 ppm), CaO (up to 5300 ppm), and FeO (up to
524 3200 ppm).

525

526 **5. Discussion**

527 **5.1. Mass Balance Calculations**

528 To judge the environmental impact of fahlore weathering, one needs to calculate the amount of each
529 element fixed in the weathering assemblage versus what is released into the fluid. First, one should
530 consider some uncertainties. A certain volume of fahlore needs to be compared to the same volume
531 of its weathering product(s). The volume of the weathering product(s) can be equal, larger or smaller
532 depending on the density of the new phases and whether components were added or lost. Textural
533 criteria are here especially important. In the observed textures of stage 1 are no cracks along or in
534 front of the finger-like tubes and the colloidal phases with irregularly arranged porosity gaps suggest
535 that they formed with only a small volume reduction. The observed weathering stage 2 preserves the
536 habit and Bi-zonation of the original fahlore and includes irregular areas with high porosity;
537 therefore, a volume reduction can be assumed as well. Stage 4 weathering produces fractures
538 throughout the fahlore and beyond into the host rock. These fractures are partially filled with
539 secondary minerals. Therefore, stage 4 weathering textures cannot be used for a quantification of
540 element mobility. Qualitatively, it is obvious that Cu and As are mobile in these stage 4 fluids and
541 leave the immediate vicinity of the weathered fahlore.

542 The mass balance calculation is more robust for main than for trace elements, because of the higher
543 analytical error for the latter. Small secondary phases cause nugget effects (eg., acanthite, cinnabar)
544 and, hence, a large error. Additionally, a small variation in trace elements has a bigger effect on the
545 result (e.g., 1 ppm in fahlore compared to 2 ppm in its weathering product would result in a 100%
546 addition of that element) and is, thus, not comparable to main elements. Therefore, only main
547 elements of fahlore (Cu, Fe, Zn, As, Sb, Bi, S) will be considered in the following calculations (see
548 chapter 5.2, Table 5).
549 For weathering stage 1, the mass balance calculations were performed by graphical volume
550 estimation using BSE images. The observed phases and the amount of porosity of stage 1 weathering
551 were colour coded, and their 2-dimensional surface area was considered equal to their 3-

552 dimensional volume. For the amorphous phases of stage 2, the EMPA analyses were compared
553 directly. The volumes of the phases of both stages were then recalculated using their known or
554 estimated densities (Cu-sulfide: 4.6 g/cm, Cu oxide: 4.0 g/cm, RGM: 7.4 g/cm, Bi-rich Cu arsenate: 4.4
555 g/cm, Bi-poor Cu arsenate: 4.2 g/cm) to their weighted fraction of the total volume of secondary
556 phases considering the porosity. The fraction of each phase and its respective chemical composition
557 determines the total amount of each element present in the total weathering volume. An example of
558 the mass balance calculation is shown in Fig. 14. The colour-coded picture in Fig. 14b shows an RGM
559 content of 12 % by volume which is recalculated using the mentioned densities of the phases to 20
560 wt.%. The RGM was analysed to contain 38.6 wt.% Bi, the Cu-sulfide 1.1 wt.% Bi and the Cu-oxide
561 phase 1.6 wt.% Bi. These numbers calculate to 0.50 g Bi in the RGM, 0.01 g Bi in the Cu-sulfide, and
562 0.02 g Bi in the Cu-oxide phase for each cubic centimetre, resulting in 0.53 g Bi per cubic cm of
563 weathering product. Using the density of fahlore and the analysed Bi content of 12.4 wt.% for the
564 fahlore of Fig. 14, each cubic cm of fahlore has 0.58 g Bi, resulting in 0.05 g loss of Bi (10 %) to the
565 weathering product. Due to the large error of the method it is considered to be immobile. Small
566 changes in the volume estimation of the RGM (which hosts most of the Bi) changes the result
567 significantly (1% change in RGM volume results in 5% elemental mobility). To minimise this
568 uncertainty, multiple colour-coded pictures were analysed to calculate the elemental mobility in Fig.
569 14 and the average mineral content was used in the calculations.

570

571 **5.2. Mineralogy and element mobility during the weathering stages**

572 **5.2.1. Element mobility during stage 1**

573 The investigated fahlores show an intensive primary hydrothermal zonation mostly due to their
574 variable (Sb+As)/Bi ratios. The sharp chemical zoning has a direct influence on the supergene phase
575 assemblages formed during stages 1: If fahlore compositions during stage 1 weathering are
576 compared to the composition of stage 1 veinlets, differences in RGM mineralogy emerge. If bismuth
577 exceeds 0.12 apfu, the weathering textures contain the Bi-Sb-bearing RGM (assemblage 1.1; Fig.
578 12b). This only holds true, if also Sb is present in the fahlore. In zones, where the Bi-content is lower,
579 tripuhyite/hydroxyferroroméite develop instead (assemblage 1.2). When fahlore contains less than
580 0.56 apfu Sb at high Bi contents (>10%), the Bi-Fe-bearing RGM forms (assemblage 1.3; Fig. 12b). As
581 As-dominated zones are very thin in the samples studied (Fig. 12a) their weathering is overprinted by
582 the neighbouring high-Bi fahlore and no statement can be made regarding their specific weathering
583 behaviour.

584 Calculation of stage 1 element mobility shows that about one third of the Cu of the secondary
585 assemblage must have been added from an external source (Fig. 14c). Zinc was completely, As and S
586 partially (80-90% and 60-80%, respectively) lost. Different behaviour in element mobility is observed
587 for Fe and Sb, depending on initial fahlore composition. Both elements behave almost immobile if
588 fahlore is Bi-rich. In Bi-poor fahlore, however, more than half of the Fe and Sb of the fahlore is
589 released into the fluid, indicating that Bi stabilizes the RGM phase. Bi behaves basically immobile in
590 all investigated stage 1 assemblages.

591 If fahlore contains elevated Ag contents, nm- to µm-sized acanthite grains are found between the Cu-
592 sulfides of stage 1 (or enclosed in the amorphous phase of stage 2). In a sample from Freudenstadt,
593 acanthite was found next to a fahlore zone with 6000 ppm Ag; no acanthite was found in the next
594 fahlore zone which contains 2000 ppm Ag. In a sample containing 4300 ppm to 8500 ppm Hg in
595 fahlore, small cinnabar grains were found in between the Bi-Sb-bearing RGM. Hence, Ag and Hg can
596 be regarded to behave mostly immobile during stage 1 weathering.

597 Although trace element mobility during weathering cannot be quantified (see section 5.1), some
598 qualitative estimation can be made. From Fig. 13a, it is obvious that at least 90% of the fahlore's Co is
599 lost during stage 1 and 2 weathering. The Co content retained during stage 1 is mostly found in the
600 Cu-sulfide or Cu-oxide phases, whereas the RGM contains an order of magnitude less Co. Manganese
601 and vanadium are about 1 to 2 orders of magnitude higher in the weathering assemblage 1
602 compared to fahlore (Fig. 13b), proving that they were added from an external source by the
603 weathering fluid, whereas stage 2 assemblage has concentrations similar to fahlore – hence, Mn and
604 V are immobile during this stage. In stage 1, Mn, V, Cr, and Pb (Fig. 13b, Table 3) are mostly retained
605 in the RGM, but unfortunately, no conclusion about Cr and Pb mobility can be drawn from the data.

606 During weathering stage 1, Si was added to form quartz. It precipitated first, as it occurs always in the
607 centre of the veinlets and the Bi-Sb-bearing RGM overgrows it.

608

609 **5.2.2. Element mobility during stage 2**

610 Calculation of the stage 2 element mobilization from all investigated samples shows that almost no
611 As is mobilized during the formation of the amorphous phase (Fig. 14d). The most striking feature of
612 stage 2 weathering is the survival of the fahlore zonation caused by Bi in the supergene amorphous
613 arsenate phase (Fig. 6). Bismuth-rich zones show no mobilization of Bi, but Bi-poor zones show an
614 apparent addition (Fig. 14d). This is, however, most likely an effect of the low concentration of Bi and
615 hence of the larger error of the method (Freudenstadt sample: 0.1-2.4 wt.% Bi in low Bi-fahlore, 0.2-
616 3.8 wt.% Bi in amorphous phase). Taking the zonation shown in Fig. 6 into account, it is unlikely that

617 significant amounts of Bi were mobilized and hence, it can be assumed that Bi is immobile also in the
618 low-Bi zones. Elements that are partly mobilized in all investigated samples are Cu (approximately a
619 third) and Sb (approximately half), whereas Zn and S are almost completely mobilized. The only S
620 remaining in stage 2 are sulfides of Ag and Hg and some sulfate to form barite. Elements added are
621 Fe (up to 110% more than previously incorporated in fahlore) and Ba to form barite. Cu-bearing
622 amorphous arsenates have also been described next to fahlore from the Clara mine (Schwarzwald,
623 Germany, Walenta 1992), Špania Dolina-Piesky and L'ubietová-Svätodušná (Slovakia, Borčinová
624 Radková et al., 2017), Mount Cervandone (Swiss-Italian border, Guastoni et al., 2006), Cínovec (Czech
625 Republic, Pauliš et al., 2008), and Mt. Pleasant (Canada, Petrunic et al., 2009) showing that it typically
626 forms during fahlore weathering, even in a wide variety of geological settings and in variable host
627 rocks.

628

629 **5.2.3. Element mobility during stage 3**

630 Stage 3 is a local weathering stage which mostly affects the older weathering assemblage and not the
631 original fahlore. Therefore, no mass balance calculation was done. The assemblage itself shows that
632 Si was externally derived to form Cu-silicates in the Königswart samples (Table 4). In Neubulach it
633 shows that the Cu-oxide phase and the Cu-sulfides are dissolved and, hence, Cu and S are mobile.
634 The formation of the amorphous Cu-arsenate-sulfate also records the mobility of As during this
635 stage.

636

637 **5.2.4. Element mobility during stage 4**

638 Stage 4 weathering minerals (e.g., azurite, mixite group minerals, bariopharmacosiderite) are
639 spatially not directly related to fahlore and only in exceptional cases, they replace older weathering
640 products. Hence, a mass balance calculation is not meaningful. The mineral assemblage, however,
641 shows that Ca, Si, Ba, Al, and C must have been added from external sources. The dissolution of host
642 rock (limestone, clastic redbeds, granite) and gangue (barite, quartz, fluorite) delivers elements like
643 C, Si, Ba, Al and Ca. This is particularly striking at Neubulach, where stage 4 minerals are (due to the
644 limestone relics on top of the deposit) Ca- or carbonate-dominated.

645 Copper to form azurite could be partially derived from older weathering products of stage 1 and 2, as
646 stage 4 minerals were observed to replace them (Fig. 11d). This would indicate that during this stage
647 also As, Bi, Sb, and Fe are released from earlier weathering assemblages, which could represent the
648 formation of the commonly occurring stage 4 mixite group minerals or bariopharmacosiderite. The

649 only Sb-bearing phase is the dusserite-arsenogorceixite solid-solution from Freudenstadt. Possibly, at
650 other localities, especially Neubulach, where dissolution of stage 2 was observed and no secondary
651 Sb minerals are known besides the RGM according to Walenta (1992), both elements were released
652 into the fluid during this weathering stage.

653 The mineral assemblage shows that during stage 4, Cu, As, Bi, Sb, and Fe are mobile. As discussed
654 above, the source of these elements is probably the dissolution of older weathering assemblages
655 (e.g., stages 1 and 2). A renewed dissolution of fahlore to form stage 4 minerals was not observed,
656 but cannot be ruled out. Also, weathering of other minerals of the primary mineral assemblage (e.g.,
657 chalcopyrite, emplectite, arsenides) could deliver elements like Cu, Bi, or As, to form stage 4
658 minerals.

659 Stage 4 minerals cover much larger areas than the previous weathering stages. Therefore, they
660 record the widespread mobilization of elements (e.g., Cu and As) which originated from fahlore. This
661 mobilization is therefore visually the most obvious weathering stage (e.g., ESM Fig. 2a). Other
662 deposits with large amounts of fahlore comprise a similarly large variety of Cu-bearing arsenates as
663 observed at the localities investigated (see Markl, 2015, for mineral lists of these deposits). Other
664 typical and well-known occurrences of such rich supergene arsenate assemblages include the Clara
665 mine (Schwarzwald, Germany; Markl 2015), Tsumeb (Namibia; Bowell 2014), or Bou Skour (Morocco,
666 Dietrich et al., 1969) to name just a few.

667

668 **5.3. The process of fahlore weathering**

669 Weathering of fahlore produces characteristic replacement textures observed independent of
670 deposit type, initial fahlore chemistry, or weathering assemblage (Nickel et al., 2007; Petrunic et al.,
671 2009; Borčinová Radkova et al., 2017; Mills et al., 2017). As described above, two types can be
672 distinguished: (1) A network of finger-/tube-like conduits infiltrating the fahlore without a visible
673 fracture and (2) a replacement front proceeding through the fahlore. Type (1) is the only type found
674 in stage 1 weathering, whereas both types are found in stage (2) where, however, the replacement
675 front is dominant. This difference implies that different processes take place during both stages.

676 The formation of secondary phases during weathering and/or alteration in general can be due to
677 incongruent dissolution (scorodite dissolution; Harvey et al., 2006), dissolution and re-precipitation in
678 an aqueous solution (weathering of electrum, Mann, 1984), support by bacteria (sulfide conversion
679 to schwertmannite; Dockrey et al., 2014), or reaction of an aqueous solution with the primary
680 mineral to form a gel-like fluid in which later secondary phases may crystallize by dehydration
681 (hematite from poorly crystalline ferrihydrite; Cudennec and Lecerf, 2006). An incongruent

682 dissolution during fahlore weathering can be excluded based on the observed textures (e.g., finger-
683 like tubes) and based on the fact, that during incongruent dissolution, the primary phase is
684 successively coated by the secondary phases thus significantly reducing its reactivity (Harvey et al.,
685 2006). No secondary coating of any phase was observed around fahlore. A bacterial influence is also
686 unlikely to explain the observed textures and complex intergrowth of secondary phases.

687 The observed textures of weathering stages 1 and 2 (Figs. 1 to 8) show colloform layered aggregates.
688 Stage 2 phases are X-ray amorphous but partly include nm-sized crystals. Raman analyses identified
689 arsenate but also water within the amorphous phases of stage 2. The textures combined with the
690 analytical results indicate that the weathering product of fahlore forms a gel-like phase, which is in
691 this case a hydrous amorphous phase which could contain nm-sized crystals or from which nm-sized
692 crystals formed due to dehydration during a later stage. The stage 1 assemblage was shown to be
693 completely crystalline, although the textures support also a crystallization from a gel. In this case, the
694 crystallization starts from the centre of the tube and from its margin, forming nm-sized crystals of Cu-
695 sulfides and the Bi-Sb-Fe phase gradually increasing in size towards the inner mantle of the tube. As
696 there are no hydrous phases observed, it can be assumed that the crystallization was initiated by
697 dehydration of the gel.

698 Fracture patterns in mineral replacement reactions were investigated by Malthe-Sørenssen et al.
699 (2006) by theoretical modelling. They found that a volume reduction between reactant and product
700 during chemical processes enhances fluid penetration along contraction fractures into the reactant
701 due to a better diffusion of chemicals. Janssen et al. (2010) used ilmenite to produce alteration
702 products by the reaction with HCl-solutions of different concentrations. They concluded that a highly
703 concentrated solution alters the mineral more quickly, forming a replacement front from the outer
704 surface of the mineral. A solution of low HCl-concentration, on the other hand, forms a network of
705 finger-like veinlets and over a longer reaction time creates its own fractures due to the reaction,
706 according to the process described by Malthe-Sørenssen et al. (2006).

707 The fahlore weathering textures of stage 1 look remarkably similar to the patterns found in the low-
708 HCl-concentration experiment by Janssen et al. (2010). Along the centre of the finger-like tubes in
709 Janssens experiments runs an open crack and resembles the quartz and RGM found in the centre of
710 the stage 1 textures. The experiment by Janssen et al. (2010) with the more concentrated HCl-
711 solution replaces the mineral completely, but leaves a pattern of alternating high porosity areas with
712 inhomogeneous layers of the product. This is similar to the stage 2 textures, where inhomogeneous
713 arsenate phases alternate with high porosity areas (Fig. 6a).

The experiments by Janssen et al. (2010) were driven by different HCl concentrations in the fluid and therefore different acidity. In the case of the fahlore weathering, the driving force for the formation of new phases is the oxidation potential of the weathering fluid (see next section 5.4). It is therefore likely, that the stage 1 weathering assemblage formed by reaction with a fluid of lower oxygen fugacity than stage 2, and hence can explain the similarities to the textures found in the experimental observations.

Similar tube-like weathering or alteration textures have also been observed in the study on ilmenite by Janssen et al. (2010), in basaltic glass on the sea floor (Fig. 2 in Dultz et al., 2014), in galena forming quartz, acanthite, and native Au in the assemblage (Fig. 5 in Kamenov et al., 2013), and in native Bi, wittichenite, emplectite, pyrite, gersdorffite, and nickeline in samples investigated in the course of this study. Hence, this short compilation is a very general, basic process reflected in always similar textures in a large variety of native elements, oxide, sulfide and arsenide minerals.

5.4. Redox processes on the deposit-scale

During fahlore weathering, Cu, As, Fe, Sb and S are increasingly oxidized from stage 1 to stage 4 reflecting a stepwise change of the oxidation potential of the weathering fluids interacting with the ore deposit. In the primary deposit, fahlore and the other sulfides are in equilibrium with the surrounding minerals and fluids and no oxidation processes take place. Hence, the elemental budget remains constant. During weathering of stage 1, the surrounding environment of the ore body changes to moderate oxygen fugacity producing the stable assemblage of oxides and sulfides. A moderate oxidation potential is also supported by the finger-like appearance of the weathering phases as discussed above (chapter 5.3). The loss of 60-80 % of sulfur during the first stage reveals that sulfur is most likely partially oxidized to sulfate and transported away besides the precipitation as S^{2-} in the Cu-sulfides. This implies that f_{O2} during this stage is somewhere around the sulfide-sulfate transition. Antimony and Fe in fahlore (Sb^{3+}, Fe^{2+}) are oxidized to Sb^{5+} in the RGM phases, and to Fe^{3+} in tripuhyite (in hydroxyferroroméite, it is reported to be Fe^{2+}, Mills et al., 2017). Stable Sb^{5+} (and Fe^{3+}) compounds in similar environments were also reported by Leverett et al. (2012) and Borčinová Radková et al. (2017). In contrast to As and Sb, Bi stays in its most stable 3+ oxidation state (Whitmire, 2013). The fact that no arsenates are formed during stage 1 implies that As probably stays in its 3+ oxidation state and is therefore mobile and rapidly lost during this initial weathering stage as shown by the mass balance calculations in chapter 4.2. This observable difference in oxidation behaviour of Sb and As follows the general oxidation potentials of both metals (Norman, 1998).

746 The change from a reducing to a more oxidized environment occurs when ore deposits are exposed
747 to near surface environments, for example by erosional processes. Also an increasing amount of
748 meteoric fluids, e.g., due to climatic variations, can result in deeper infiltration of oxidized fluids (Park
749 and MacDiarmid 1975). The change from reduced to more oxidized conditions during weathering
750 stage 1 is likely to reflect the transition of the primary ore body to the cementation zone and
751 therefore a general change also in the vein-hosting fluid aquifers.

752 Weathering stage 2 records a more aggressive fluid which is far from equilibrium with the fahlore.
753 The occurrence of arsenates and the absence of Cu-sulfides reflects higher oxygen fugacities than
754 during stage 1. Such assemblages are typical of oxidation zones of hydrothermal ore deposits
755 (Magalhaes et al., 1988). The oxidation potential during this stage, however, is not high enough to
756 alter stage 1 (e.g., the sulfides), since both assemblages coexist.

757 The partial loss of Cu in stage 2 and the addition of Cu in stage 1 could point to mobilization of Cu
758 from upper parts of the weathering profile (e.g., oxidation zone) down to the cementation zone, or
759 an evolution of the fluid from a stage 2 fluid towards a stage 1 fluid. For such a fluid evolution,
760 however, there is no textural evidence on the small scale; rather, it appears to be a process on the
761 scale of a deposit. An opposite evolution of a stage 1 towards a stage 2 fluid by fluid-mineral
762 interaction can be ruled out as during stage 1, oxygen is consumed and hence, the f_{O2} in the fluid
763 decreases – stage 2 phases, however, require an increased f_{O2} (see above).

764 In contrast to the earlier in-situ stages, stage 1 and 2 phases are dissolved during stages 3 and 4, the
765 solution is transported away and newly formed minerals occur in cracks, fill empty voids or brecciate
766 former weathering stages. Besides the textural change of the weathering products, also a chemical
767 change of the weathering phases can be observed: during stage 3 and 4, mostly carbonates and Cu-,
768 Ca-, Ba-, and/or Al-Arsenates are formed. This shows the change from an in-situ controlled (more or
769 less closed?) system to an open system, and the strong mobility of elements could reflect the gossan
770 in the classical weathering profile of ore deposits.

771 Hence, the temporal evolution of fahlore weathering textures reflects the transition from fresh ore
772 to cementation zone, oxidation zone and finally gossan textures and assemblages in one hand
773 specimen. One fahlore grain can, thus, record the uplift and erosion of an ore deposit and the
774 increasing fluid/rock interaction of a weathered ore deposit with time.

775

776 **6. Summary and conclusions**

777 The weathering of Bi-bearing tennantite-tetrahedrite solid-solution can be classified in four
778 subsequent stages based on texture, mineralogy, and composition:

1. The first stage forms irregular finger-like veinlets within fahlore with crystalline Cu-sulfides and minerals of the roméite group (RGM) in a crystalline Cu-oxide groundmass. The chemistry of the RGM is dependent on the fahlore chemistry. During this stage, most of Zn and some of As and S of the fahlore is mobile and lost to the fluid. External Si is added to form quartz during this stage. In Bi-rich fahlore Fe, Bi and Sb are immobile and captured in the RGM, whereas Bi-poor fahlore releases parts of its Fe and Sb to the environment upon weathering. Sulfur is partly immobile and fixed in Cu-sulfides. The secondary sulfides and the addition of Cu suggest that these textures reflect the cementation zone of a classical weathering profile, in which only some elements are already oxidized (e.g., Sb, Fe).

2. This stage forms reaction fronts through the fahlore composed of amorphous to nano-crystalline porous Cu-arsenates. Arsenic is immobile during this stage, whereas most of the S, Zn, and Sb is transported away by the fluid. Iron, together with Ba, is added to the assemblage. Bismuth is also immobile during this stage and is incorporated in the arsenate phase; the Bi-zonation of the primary fahlore is retained. This stage is typical of the oxidation zone due to the complete oxidation of the remaining elements (i.e., Cu, S, As).

3. This stage is locally restricted and not part of the general process, but represents micro compartments. In the Neubulach samples, stage 3 partly dissolves previous weathering assemblages and crystallized a minor Cu-arsenate-sulfate assemblage. In Königswart samples, older weathering assemblages were brecciated and cemented by amorphous Cu-silicates. The assemblages show that Si, Cu, and As are mobile during this stage.

4. This stage is spatially independent from fahlore and secondary minerals form on fractures and partly fill the voids of stage 3. Their mineralogy is dependent on the hydrothermal assemblage and the local host rocks. Calcium- or carbonate-bearing minerals, for example, are most abundant in vicinity to limestones (Neubulach). This stage represents a typical gossan mineralization with a widespread mobilization of metals as it is also observed at the Clara mine (Schwarzwald, Germany; Markl, 2015), from Tsumeb (Namibia; Bowell, 2014), and Bou Skour (Morocco, Dietrich et al., 1969).

The physical process of weathering reflects the chemical gradient between fahlore and meteoric fluid. During stage 1 in the cementation zone, the chemical gradient (i.e. redox potential) and the fluid/mineral ratio is low. This causes the formation of finger-like tubes, filled by a gel-like phase which then dehydrates and crystallizes. These textures are very similar to textures found by experimental alteration of ilmenite by low-concentrated acid. In the oxidation zone, the chemical gradient between fluid and fahlore and the fluid/mineral ratio is higher; reaction fronts overprint the fahlore in this stage 2 and record a process that is probably orders of magnitude faster than formation of stage 1. These textures are also very similar to textures found by experimental alteration of ilmenite, but in this case by high-concentrated acid. In the final stages 3 and 4, the

chemical gradients and fluid/mineral ratios are greatest, and secondary minerals form spatially independent from the original fahlore location.

Bismuth is retained in the weathering products during stages 1 and 2. Bi-rich secondary minerals like mixite, bismutite or atelestite formed during stage 4 only at localities, where native Bi or Bi-Cu sulfides (wittichenite, emplectite) are abundant. These phases, in contrast to fahlore, obviously release Bi to weathering fluids.

The observed textures of stage 1 are reported from other weathering environments and from a variety of native elements, oxide, arsenide and sulfide phases. This indicates that in weathering environments with a low redox- or chemical potential in general, diffusive weathering processes are very common. This is clear evidence for the fact, that the diffusive process during the first contact with oxidizing fluids to form cementation zone assemblages is a very basic process and not only valid for fahlore.

Acknowledgments

We are grateful to T. Wenzel, C. Berthold, H. Schulz, T. Kiemle (all from Tübingen), and S. Gilbricht (Freiberg) for analytical help and S. Schafflick (Tübingen) for the great sample preparation. J. Harsch and M. Schlaich are thanked for help during the early study of the project and T. Wenzel (Tübingen) for discussions, comments and an initial review of the draft manuscript. This work is a contribution of the r^4 project "ResErVar—Ressourcenpotential hydrothermaler Lagerstätten der Varisziden" funded by the German Ministry of Education and Research (BMBF; Project reference number 033R129E).

834 **References**

835 Arroyo Y. R. R. and Siebe C. (2007) Weathering of sulphide minerals and trace element speciation in
836 tailings of various ages in the Guanajuato mining district, Mexico. *Catena* **71**(3), 497-506.

837 Atencio D. Andrade M. B. Christy A. G. Gieré R. and Kartashov P. M. (2010) The pyrochlore
838 supergroup of minerals: nomenclature. *Can. Mineral.* **48**(3), 673-698.

839 Bachmann K. Frenzel M. Krause J. and Gutzmer J. (2017) Advanced identification and quantification
840 of In-bearing minerals by scanning electron microscope-based image analysis. *Microsc. Microanal.*
841 **23**, 527-537.

842 Baggio S. B. Hartmann L. A. Lazarov M. Massone H. J. Opitz J. Theye T. and Viefhaus T. (2018) Origin
843 of native copper in the Paraná volcanic province, Brazil, integrating Cu stable isotopes in a multi-
844 analytical approach. *Miner. Deposita* **53**, 417-434.

845 Berthold C. Bjeoumikhov A. and Brügemann L. (2009) Fast XRD^2 Microdiffraction with Focusing X-Ray
846 Microlenses. *Part. Part. Syst. Char.* **26**, 107-111.

847 Biskupek J. and Kaiser U. (2004) Practical considerations on the determination of the accuracy of the
848 lattice parameters measurements from digital recorded diffractograms. *J. Electron Microsc.* **53**(6),
849 601-610.

850 Bliedtner M. and Martin M. (1986) *Erz- und Minerallagerstätten des Mittleren Schwarzwaldes.* LGRB,
851 Freiburg. pp. 786.

852 Bons P. D. Fusswinkel T. Gomez-Rivas E. Markl G. Wagner T. and Walter B. (2014) Fluid mixing from
853 below in unconformity-related hydrothermal ore deposits. *Geology* **42**, 1035-1038.

854 Borčinová Radková A. Jamieson H. Lalinská-Voleková B. Majzlan J. Števko M. and Chovan M. (2017)
855 Mineralogical controls on antimony and arsenic mobility during tetrahedrite-tennantite weathering
856 at historic mine sites Špania Dolina-Piesky and Ľubietová-Svätodušná, Slovakia. *Am. Mineral.* **102**(5),
857 1091-1100.

858 Bowell R. J. (2014) Hydrogeochemistry of the Tsumeb deposit: Implications for arsenate mineral
859 stability. *Rev. Mineral. Geochem.* **79**, 589-627.

860 Breskovska V. and Tarkian M. (1994) Compositional variation in Bi-bearing fahlores. *Neues JB. Miner.*
861 *Monat.* **5**, 230-240.

862 Bucher K. Zhu Y. and Stober I. (2009) Groundwater in fractured crystalline rocks, the Clara mine,
863 Black Forest (Germany). *Int. J. Earth Sci.* **98**(7), 1727-1739.

864 Burisch M. Walter B. F. Wälle M. and Markl G. (2016) Tracing fluid migration pathways in the root
865 zone below unconformity-related hydrothermal veins: Insights from trace element systematics of
866 individual fluid inclusions. *Chem. Geol.* **429**, 44-50.

867 Burmann F. Keim M. F. Oelmann Y. Teiber H. Marks M. A. W. and Markl G. (2013) The source of
868 phosphate in the oxidation zone of ore deposits: Evidence from oxygen isotope composition of
869 pyromorphite. *Geochim. Cosmochim. Acta* **123**, 427-439.

870 Christy A. G. and Atencio D. (2013) Clarification of status of species in the pyrochlore supergroup.
871 *Mineral. Mag.* **77**(1), 13-20.

872 Cudennec Y. and Lecerf A. (2006) The transformation of ferrihydrite into goethite or hematite,
873 revisited. *J. Solid State Chem.* **179**(3), 716-722.

874 Dietrich J. E. Orliac M. and Permingeat F. (1969) L'agardite, une nouvelle espèce minérale, et le
875 problème du chlorotile. *B. Soc. Fr. Mineral Cr.* **92**, 420-434.

876 Dockrey J. W. Lindsay M. B. J. Mayer K. U. Beckie R. D. Norlund K. L. I. Warren L. A. and Southam G.
877 (2014) Acidic microenvironments in waste rock characterized by neutral drainage: Bacteria-mineral
878 interactions at sulfide surfaces. *Minerals* **4**, 170-190.

879 Downs R. T. (2006) The RUFF Project: an integrated study of the chemistry, crystallography, Raman
880 and infrared spectroscopy of minerals. *Program and Abstracts of the 19th General Meeting of the*
881 *International Mineralogical Association,* Kobe, Japan, O03-13.

882 Dultz S. Boy J. Dupont C. Halisch M. Behrens H. Welsch A. M. Erdmann M. Cramm S. Helsch G. and
883 Deubner J. (2014) Alteration of a submarine basaltic glass under environmental conditions
884 conductive for microorganisms: Growth pattern of the microbial community and mechanism of
885 palagonite formation. *Geomicrobiol. J.* **31**, 813-834.

886 Fandrich R. Gu Y. Burrows D. and Moeller K. (2007) Modern SEM-based mineral liberation analysis.
887 *Int. J. Miner. Process.* **84**, 310-320.

888 Franzke H. J. and Werner W. (1994) Wie beeinflusste die Tektonik des Kristallins und des
889 Rheingrabens die hydrothermalen Gangstrukturen des Schwarzwaldes? *Abh. Geol. Landesamt Bad.-*
890 *Württ.* **14**, 99-118.

891 George L. L. Cook N. J. and Ciobanu C. L. (2017) Minor and trace elements in natural tetrahedrite-
892 tennantite: Effects on element partitioning among base metal sulphides. *Minerals* **7**(2) 1-25.

893 Geyer O. F. and Gwinner M. P. (2011) *Geologie von Baden-Württemberg.* Schweizerbart'sche
894 Verlagsbuchhandlung, Stuttgart. pp. 627.

895 Göb S. Wenzel T. Bau M. Jacob D. E. Loges A. and Markl G. (2011) The redistribution of rare-earth
896 elements in secondary minerals of hydrothermal veins, Schwarzwald, Southwestern Germany. *Can.*
897 *Mineral.* **49**, 1305-1333.

898 Göb S. Gühring J. E. Bau M. and Markl G. (2013a) Remobilization of U and REE and the formation of
899 secondary minerals in oxidized U deposits. *Am. Mineral.* **98**, 530-548.

900 Göb S. Loges A. Nolde N. Bau M. Jacob D. E. and Markl G. (2013b) Major and trace element
901 compositions (including REE) of mineral, thermal, mine and surface waters in SW Germany and
902 implications for water-rock interaction. *Appl. Geochem.* **33**, 127-152.

903 Göb S. Bau M. and Markl G. (2015) Chemical composition of waters in a former Cu-As mine: water-
904 rock interaction, REE systematics and stability of secondary copper minerals. *Neues JB. Miner. Abh.*
905 **192**(1) 11-32.

906 Gołębiowska B. Pieczka A. and Parafiniuk J. (2012) Substitution of Bi for Sb and As in minerals of the
907 tetrahedrite series from Rędziny, Lower Silesia, southwestern Poland. *Can. Mineral.* **50**(2), 267-279.

908 Guastoni A. Pezzotta F. and Vignola P. (2006) Characterization and genetic inferences of arsenates,
909 sulfates and vanadates of Fe, Cu, Pb, Zn from Mount Cervandone (Western Alps, Italy). *Period.*
910 *Mineral.* **75**, 414-150.

911 Harvey M. C. Schreiber M. E. Rimstidt J. D. and Griffith M. M. (2006) Scorodite dissolution kinetics:
912 Implication for arsenic release. *Environ. Sci. Technol.* **40**, 6709-6714.

913 Haßler K. Taubald H. and Markl G. (2014) Carbon and oxygen isotope composition of Pb-, Cu- and Bi-
914 carbonates of the Schwarzwald mining district: Carbon sources, first data on bismutite and the
915 discovery of an oxidation zone formed by ascending thermal water. *Geochim. Cosmochim. Acta* **133**,
916 1-16.

917 Hautmann S. and Lippolt H. J. (2000) $^{40}Ar/^{39}Ar$ dating of central European K-Mn oxides – a
918 chronological framework of supergene alteration processes during the Neogene. *Chem. Geol.* **170**,
919 37-80.

920 Hofmann B. and Eikenberg J. (1991) The Krunkelbach uranium deposit, Schwarzwald, Germany:
921 correlation of radiometric ages (U-Pb, U-Xe-Kr, K-Ar, ^{230}Th-^{234}U) with mineralogical stages and fluid
922 inclusions. *Econ. Geol.* **86**, 1031-1049.

923 Ixer R. A. (2001) An assessment of copper mineralization from the Great Orme mine, Llandudno,
924 North Wales, as ore in the Bronze Age. *P. Yorks. Geol. Soc.* **53**, 213-219.

925 Janssen A. Putnis A. Geisler T. and Putnis C. V. (2010) The experimental replacement of ilmenite by
926 rutile in HCl solutions. *Mineral. Mag.* **74**, 633-644.

927 Johnson N. E. Craig J. R. and Rimstidt J. D. (1986) Compositional trends in tetrahedrite. *Can. Mineral.*
928 **24**(2), 385-397.

929 Kamenov G. D. Melchiorre E. B. Ricker F. N. and DeWitt E. (2013) Insights from Pb isotopes for native
930 gold formation during hypogene and supergene processes at Rich Hill, Arizona. *Econ. Geol.* **108**,
931 1577-1589.

932 Keim M. F. and Markl G. (2015) Weathering of galena: Mineralogical processes, hydrogeochemical
933 fluid path modelling, and estimation of the growth rate of pyromorphite. *Am. Mineral.* **100**, 1584-
934 1594.

935 Keim M. F. Vaudrin R. and Markl G. (2016) Redistribution of silver during supergene oxidation of
936 argentiferous galena: A case study from the Schwarzwald, SW Germany. *Neues JB. Miner Abh.* **193**(3),
937 295-309.

938 Keim M. F. Gassmann B. and Markl G. (2017) Formation of basic lead phases during fire-setting and
939 other natural and man-made processes. *Am. Mineral.***102**(7), 1482-1500.

940 Kolitsch U. (2000) Eine durch Betoneinwirkung entstandene Paragenese von Blei-Verbindungen aus
941 der Grube Clara im mittleren Schwarzwald. *Erzgräber* **14**, 48-53.

942 Kozub G. A. (2014) Distribution of Ag in Cu-sulfides in Kupferschiefer deposits, SW Poland.
943 *Geophysical Research Abstracts* **16**, EGU2014-8944.

944 Lara R. H. Velázquez L. J. Vazquez-Arenas J. Mallet M. Dossot M. Labastida I. Sosa-Rodríguez F. S.
945 Espinosa-Cristóbal L. F. Escobedo-Bretado M. A. and Cruz, R. (2016) Arsenopyrite weathering under
946 conditions of simulated calcareous soil. *Environ.Sci. Pollut. R.* **23**(4), 3681-3706.

947 Leach D. L. Landis and G. P. and Hofstra A. H. (1988) Metamorphic origin of the Coeur d'Alene base-
948 and precious-metal veins in the Belt basin, Idaho and Montana. *Geology* **16**, 122-125.

949 Leverett P. Reynolds J. K. Roper A. J. and Williams P. A. (2012) Tripuhyite and schafarzikite: two of the
950 ultimate sinks for antimony in the natural environment. *Mineral. Mag.* **76**(4), 891-902.

Lippolt H. J. Brander T. and Mankopf N. R. (1998) An attempt to determine formation ages of goethites and limonites by (U+Th)-^{4}He dating. *Neues JB. Miner. Monat.* **11**, 505-528.

Magalhaes M. C. F. Pedrosa de Jesus J. D. and Williams P. A. (1988) The chemistry of formation of some secondary arsenate minerals of Cu(II), Zn(II) andPb(II). *Mineral. Mag.* **52**, 679–690.

Makovicky E. (2006) Crystal structures of sulfides and other chalcogenides. *Rev. Mineral. Geochem.* **61**, 7-125.

Malthe-Sørenssen A. Jamtveit B. and Meakin P. (2006) Fracture patterns generated by diffusion controlled volume changing reactions. *Phys. Rev. Lett.* **96**, 245501.

Mann A. W. (1984) Mobility of gold and silver in lateritic weathering profiles: Some observations from Western Australia. *Econ. Geol.* **79**, 38-49.

Markl G. (2005) *Bergbau und Mineralienhandel im fürstenbergischen Kinzigtal*. Markstein Verlag. Filderstadt. pp. 448.

Markl G. Marks M. A. W. Derrey I. and Gühring J. E. (2014a) Weathering of cobalt arsenides: Natural assemblages and calculated stability relations among secondary Ca-Mg-Co arsenates and carbonates. *Am. Mineral.* **99**, 44-56

Markl G. Marks M. A. W. Holzäpfel J. and Wenzel T. (2014b) Major, minor, and trace element composition of pyromorphite-group minerals as recorder of supergene weathering processes from the Schwarzwald mining district, SW Germany. *Am. Mineral.* **99**, 1133-1146.

Markl G. (2015) *Schwarzwald: Lagerstätten und Mineralien aus vier Jahrhunderten. Band 1, Nordschwarzwald und Grube Clara.* Bode Verlag, Salzhemmendorf. pp. 672.

Markl G. (2016) *Schwarzwald, Lagerstätten und Mineralien aus vier Jahrhunderten. Band 2: Mittlerer Schwarzwald Teil 1.* Bode Verlag, Salzhemmendorf. pp. 648.

Massone H. J. Opitz J. Theye T. and Nasir S. (2013) Evolution of a very deeply subducted metasediment from As Sifah, northeastern coast of Oman. *Lithos* **156**, 171-185.

Metz R. Richter M. and Schürenberg H. (1957) Die Blei-Zink-Erzgänge des Schwarzwaldes. *Geol. Jb. Beihefte* **29**, 1-277.

Metz R. (1977) *Mineralogisch-landeskundliche Wanderungen im Nordschwarzwald, besonders in desses alten Bergbaurevieren.* Moritz Schaufenburg Verlag, Lahr. pp. 277.

Mills S. J Christy A. G. Rumsey M. S. Spratt J. Bittarello E. Favreau G. Ciriotti M. and Berbain C. (2017) Hydroxyferroroméite, a new secondary weathering mineral from Oms, France. *Eur. J. Mineral.* **29**, 307-314.

Moëlo Y. Makovicky E. Mozgova N. N. Jambor J. L. Cook N. Pring A. and Balic-Žunic T. (2008) Sulfosalt systematics: a review. Report of the sulfosalt sub-committee of the IMA Commission on Ore Mineralogy. *Eur. J. Mineral.* **20**(1), 7-46.

Mueller A. G. and Muhling J. R. (2013) Silver-rich telluride mineralization at Mount Charlotte and Au-Ag zonation in the giant Golden Mile deposit, Kalgoorlie, Western Australia. *Miner. Deposita* **48**, 295-311.

Nickel E. H. Williams P. A. Downes P. J. Buchert D. E. and Vaughan D. (2007) Secondary minerals in a tennantite boxwork from the Bali Lo prospect, Ashburton Downs, Western Australia. *Aust. J. Miner.* **13**, 31-39.

Norman N. C. (1998) *Chemistry of Arsenic, Antimony and Bismuth*. Blackie Academic and Professional, London. 487 pp.

Onuk P. Melcher F. Mertz-Kraus R. Gäbler H. E. and Goldmann S. (2017) Development of a Matrix-Matched Sphalerite Reference Material (MUL-ZnS-1) for Calibration of In Situ Trace Element Measurements by Laser Ablation-Inductively Coupled Plasma-Mass Spectrometry. *Geostand. Geoanal. Res.* **41**(2), 263-272.

Park C. F. and MacDiarmid R. A. (1975) *Ore Deposits*. W.H. Freeman and Company, San Francisco. pp. 985.

Pauliš P. Novák F. Kotatko L. Jonáscaron F. Dvořák Z. and Ševcú J. (2008) Nové vyskyty nerostů na Sn-W ložisku Cínovec. *Bull. Mineralogicko-Petrologickeho Oddeleni Narodniho Muzea v Praze* 1**6**, 113-117.

Petrunic B. M. Al T. A. Weaver L. and Hall D. (2009) Identification and characterization of secondary minerals formed in tungsten mine tailings using transmission electron microscopy. *Appl. Geochem.* **24**, 2222-2233.

Pfaff K. Romer R. L. and Markl G. (2009) U-Pb ages of ferberite, chalcedony, agate, 'U-mica' and pitchblende: constraints on the mineralization history of the Schwarzwald ore district. *Eur. J. Mineral.* **21**, 817-836.

Plotinskaya O. Y. Grabezhev A. I. and Seltmann R. (2015) Fahlores compositional zoning in a porphyry-epithermal system: Biksizak occurrence, South Urals, Russia as an example. *Geol. Ore Deposit.* **57**, 42-63.

Prasad A. S. (2013) *Essential and toxic element: trace elements in human health and disease*. Elsevier. 534 pp.

Reich M. and Vasconcelos P. M. (2015) Geological and economic significance of supergene metal deposits. *Elements* **11**(5), 305-310.

Repstock A. Voudouris P. and Kolitsch U. (2015) New occurrences of watanabeite, colusite, "arsenosulvanite" and "Cu-excess" tetrahedrite-tennantite at the Pefka high-sulfidation epithermmal deposit, northeastern Greece. – *Neues JB. Miner. Abh.* **192**, 135-149.

Roper A. J. Williams P. A. and Filella M. (2012) Secondary antimony minerals: phases that control the dispersion of antimony in the supergene zone. *Geochemistry* **72**, 9-14.

Rupf I. and Nitsch E. (2008) Das Geologische Landesmodell von Baden-Württemberg: Datengrundlagen, technische Umsetzung und erste geologische Ergebnisse. *LGRB Information* **21**, 1-82.

Staude S. Bons P. D. and Markl G. (2009) Hydrothermal vein formation by extension-driven dewatering of the middle crust: An example from SW Germany. *Earth Planet. Sc. Lett.* **286**, 387-395.

Staude S. Mordhorst T. Neumann R. Prebeck W. and Markl G. (2010) Compositional variation of the tennantite-tetrahedrite solid-solution series in the Schwarzwald ore district (SW Germany): The role of mineralization processes and fluid source. *Mineral. Mag.* **74**(2), 309-339.

Staude S. Göb S. Pfaff K. Ströbele F. Premo W. R. and Markl G. (2011) Deciphering fluid sources of hydrothermal systems: A combined Sr- and S-isotope study on barite (Schwarzwald, SW Germany). *Chem. Geol.* **286**, 1-20.

Staude S. Werner W. Mordhorst T. Wemmer K. Jacob D. E. and Markl G. (2012a) Multi-stage Ag-Bi-Co-Ni-U and Cu-Bi vein mineralization at Wittichen, Schwarzwald, SW Germany: geological setting, ore mineralogy, and fluid evolution. *Miner. Deposita* **47**, 251-276.

Staude S. Mordhorst T. Nau S. Pfaff K. Brügmann G. Jacob D. E. and Markl G. (2012b) Hydrothermal carbonates of the Schwarzwald ore district, Southwestern Germany: Carbon source and conditions of formation using $\delta^{18}O$, $\delta^{13}C$, $^{87}Sr/^{86}Sr$, and fluid inclusions. *Can. Mineral.* **50**, 1404-1434.

Vavelidis M. and Melfos V. (2004) Bi–Ag-bearing tetrahedrite-tennantite in the Kapsalina copper mineralisation, Thasos Island, Northern Greece. *Neues JB. Miner. Abh.* **180**(2), 149-169.

Villinger E. and Zedler H. (2006) *Geologische Karte des Schwarzwaldes 1:150 000*. LGRB, Freiburg.

Walenta K. (1983) Bismutostibiconite, ein neues Mineral der Stibiconitgruppe aus dem Schwarzwald. *Chem. Erde* **42**, 77-81.

Walenta K. (1992) *Die Mineralien des Schwarzwaldes*. Weise Verlag, München. pp. 336.

Walter B. F. Burisch M. and Markl G. (2016) The long-term chemical evolution of continental basement brines – a field study from the Schwarzwald, SW Germany. *Geofluids* **16**, 604-623.

Walter B. F. Burisch M. Fusswinkel T. Marks M. A. W. Steele-MacInnis M. Wälle M. Apukhtina O. B. and Markl G. (2018) Multi-reservoir fluid mixing processes in rift-related hydrothermal veins, Schwarzwald, SW-Germany. *J. Geochem. Explor.* **186**, 158-186.

Walter B. F. Gerdes A. Kleinhanns I. C. Dunkl I. von Eynatten H. Kreissl S. and Markl G. (in press) The connection between hydrothermal fluids, mineralization, tectonics and magmatism in a continental rift setting: fluorite Sm-Nd and hematite and carbonates U-Pb geochronology from the Rhinegraben in SW Germany. *Geochim. Cosmochim. Acta.*

Werner W. and Dennert V. (2004) *Lagerstätten und Bergbau im Schwarzwald*. Landesamt für Geologie, Rohstoffe und Bergbau Baden-Württemberg, Freiburg. pp. 334.

Werner W. (2012) Schätze unter dem Boden: Was wissen wir über die tiefliegenden Rohstoffe in Baden-Württemberg? *Ber. Naturf. Ges. Freiburg i. Br.* **102**, 37-92.

Whitmire K. H. (2013) *Bismuth: Inorganic Chemistry*. Encyclopedia of Inorganic and Bioinorganic Chemistry. John Wiley & Sons 1–32. DOI: 10.1002/9781119951438.eibc0018.pub2

Wohlgemuth-Ueberwasser C. C. Viljoen F. Petersen S. and Vorster C. (2015) Distribution and solubility limits of trace elements in hydrothermal black smoker sulfides: An in-situ LA-ICP-MS study. *Geochim. Cosmochim. Acta* **159**, 16-41.

Wu I. and Petersen U. (1977) Geochemistry of tetrahedrite and mineral zoning at Casapalca, Peru. *Econ. Geol.* **72**(6), 993-1016.

Zhu Y. Merkel B. J. Stober I. and Bucher K. (2003) The hydrogeochemistry of arsenic in the Clara mine, Germany. *Mine Water Environ.* **22**(3), 110-117.

Figure captions

Figure 1

BSE and chemical maps of a stage 1 weathering in zoned fahlore from Neubulach. (a) BSE image showing fahlore with zonation of its Bi content and finger-like tubes where weathering assemblages are situated. Note the bright weathering products coincides where fahlore is bright. (b). Close-up of (a) showing the Bi contents of the fahlore zonation and the complex weathering assemblages of stage 1. A younger vein contains stage 4 weathering phases. (c) Map of Cu of (b). In areas where the Bi content of the fahlore is low the weathering assemblage 1 contains more covellite (bright red). (d) Map of As of (b) showing the lack of As in weathering stage 1 (dark) and arsenate minerals of stage 4 (bright blue line through stage 1). (e) Map of Bi of (b) showing the Bi-zonation in fahlore and the enrichment of Bi in stage 1 assemblage only where Bi is elevated in fahlore. (f) Map of Sb of (b) showing a Sb-enrichment in stage 1 assemblage. Where Bi-rich fahlore hosts the weathering assemblage Sb is found in the Bi-Sb-Fe phase, whereas where hosted by Sb-rich fahlore the Sb-Fe phase is formed. Note, all EDS elemental maps are false-colour images and colour intensity represents the distribution of each element.

Figure 2

Reflected light photomicrograph in oil, showing different Cu-sulfides of weathering stage 1 from Neubulach.

Figure 3

TEM images of stage 1 weathering from Neubulach. (a) High-angle annular dark field (HAADF) STEM image of fahlore in contact to weathering assemblage. Note the zonation within the weathering assemblage, partly due to Cu-sulfide (CuSulf) occurence. (b) STEM HAADF close up of (a) showing the distribution of Cu-sulfide and the RGM in a Cu-oxide (CuOx) groundmass. (c) STEM EDS map of Bi of (b) showing the distribution of the RGM. (d) STEM EDS map of As of (b). Note the concentration of As in small veinlets, that represent phase and grain boundaries. (e) BSE image showing the location of the two textures shown in (b-d) and (f, g), respectively. (f) STEM HAADF image showing the spatial relation between Cu-sulfides and RGM, both elongate, in a Cu-oxide groundmass. (g) STEM EDS map of Cu and Bi of (f). The circular inset shows the position of the SAD aperture used to obtain the diffraction pattern in the ESM Fig. 6. Note, all STEM EDS elemental maps are false-colour images and

1096 colour intensity represents the distribution of each element but is also dependent on sample
1097 thickness.

1098

1099 **Figure 4**

1100 Processed mineral liberation analysis (MLA) image of fahlore with Bi-poor zones (dark grey) and Bi-
1101 rich zones (grey) cut by weathering stage 1. The weathering assemblage is colour coded to show the
1102 dominant mineral in each pixel (pixel size: 0.25 by 0.25 µm). As the analytical beam excitement
1103 volume is much larger than the pixel size only areas of the dominant mineral can be shown.

1104

1105 **Figure 5**

1106 (a) BSE image showing finger-like weathering assemblage inside and a replacement front outside
1107 native Bi from Wittichen. Both phases are bismite. (b) Transmitted light photo of native Bi from
1108 Wittichen which is replaced by a front of bismite which then later is cut by a mixite vein. Note the
1109 zonation of bismite. (C) Finger-like weathering assemblage in wittichenite and emplectite from
1110 Wittichen.

1111

1112 **Figure 6**

1113 (a) BSE image of weathering stage 2 from Freudenstadt, which is cut by younger stage 4 minerals.
1114 The Bi-concentration of fahlore and the weathering product, analysed by EMPA, are shown. (b) Map
1115 of S of (a) showing distribution of fahlore. (c) Map of Bi of (a) showing the Bi zonation of fahlore and
1116 in the stage 2 weathering assemblage. (d) BSE image of neighbouring fahlore and chalcopyrite
1117 showing stage 1 and 2 weathering from Neubulach. (e) Map of Sb and As showing the distribution of
1118 weathering stage 1 of fahlore by Sb, which is only minor in chalcopyrite. Stage 2 weathering,
1119 represented by As, is mostly found in chalcopyrite.

1120

1121 **Figure 7**

1122 Detail study of regions shown in Fig. 6a. (a) BSE magnified from Fig 6a highlighting the areas
1123 investigated by TEM in (b-f) from weathering stage 2. (b) Bright field image of the dark zone in (a)
1124 showing colloidal appearance of the phases present. (c) Selected area diffraction pattern of the
1125 central region in (b). The diffusive halo and the absence of discrete diffraction spots is characteristic

for amorphous material. (d) STEM HAADF image of the bright zone in (a) showing nm-sized phases in a groundmass. (e) EDS map of Ag, Bi, and Cu showing the spatial relation between a 50 nm-sized Ag-sulfide crystal and the less than 10 nm-sized Cu-oxides in a Cu-arsenate groundmass. Bismuth is homogeneously distributed and appears to be amorphous. (f) Selected area diffraction pattern of the central region in (d) indicating the nano-crystalline structure of some phases. Furthermore, a diffuse halo indicates the presence of amorphous material.

Figure 8

(a) BSE image of fahlore weathered by stage 2 which includes µm-sized Ag-sulfide aggregates. Note the difference in Bi-concentration of the fahlore is reflected in the secondary arsenate. (b) BSE image overlain by map of As and Hg showing the distribution of stage 1 weathering, represented by the Bi-Sb-Fe phase and HgS and of stage 2 weathering, represented by As and barite.

Figure 9

(a) and (b) Combined reflected and transmitted light photo of weathering stages 1 to 3 from Neubulach. Stage 1 is characterized by a high Cu-sulfide content which is missing in stages 2 and 3. Stage 2 is composed of alternating layers of a Cu-arsenate and barite (highlighted in inlet of (a) in BSE mode; white: barite; grey: Cu-arsenate). Stage 3 is subdivided into a green phase on the contact to stage 1 and a yellow phase. (c) BSE image of (b) showing the transition from the stage 1 to stage 3 weathering. (d) Close-up of (c) showing Cu-sulfides (CuS) in stage 1 weathering assemblage and a porous phase in the green stage 3 assemblage, all intergrown with the Bi-Sb-Fe phase.

Figure 10

(a) BSE image of stages 2 to 4 weathering from Königswart. (b) Map of Ba, Si, and Bi of (a). Clasts with weathering assemblage 2 are overgrown by a Si-bearing phase and subhedral quartz which is in turn cut by barite of stage 4.

Figure 11

(a) BSE image of stage 4 weathering which cuts through stage 1 from Neubulach (see Fig. 1). (b) Map of Cu and Ba of (a) showing the cyclic intergrowth of bariopharmacosiderite and azurite. (c) Azurite

vein of stage 4 cutting through quartz and where it intersects older weathering stages forms an unknown Ca-Cu-bearing arsenate (transmitted light photograph). (d) Azurite of stage 4 replaces parts of stage 1 assemblage and completely stage 2. Whether the partly dissolution of stage 1 is part of stage 3 (compare Fig. 9) or whether it is a direct replacement in stage 4 is unclear. In both stages the Bi-Sb-Fe phase is preserved.

Figure 12

(a) Variation of As-Sb-Bi of the investigated fahlore. Most samples show As-Bi exchange, whereas the Sb-content characteristic for each vein system. The Sb-rich and Bi-free fahlore from Wittichen occurred as small older inclusions in the As-Bi-bearing fahlore and did not show effects of weathering. (b) Same dataset of (a) but only showing analyses where fahlore is cut by stage 1 weathering assemblage and colour coded by the oxide phase neighbouring this fahlore. (c) Concentration of As and Cu of the amorphous stage 2 phase (calculated to 100 atom % without volatiles).

Figure 13

(a) Co versus Zn and (b) V versus Mn concentrations from LA-ICP-MS analyses of fahlore and weathering products of stages 1-4. Minerals of stage 4 are labelled, whereas other analyses represent mixed or amorphous phases. Fahlore has higher Zn and Co but lower Mn and V concentrations compared to their weathering products. Stage 3 of Neubulach is represented by dissolution of Cu-sulfides and Cu-oxides leaving the roméite group mineral (RGM) behind. Comparing this phase with the overall stage 1 assemblage the RGM has lower Co, but higher Mn, and V concentrations.

Figure 14

(a) BSE image of a representative stage 1 assemblage from Neubulach. (b) Colour coded picture of (a) to highlight each phase and its quantity of this weathering stage (CuOx: Cu oxide, CuSulf: Cu-sulfide, RGM: roméite group mineral). (c) Results of stage 1 mass balance calculation presented in Table 4 from Neubulach and Freudenstadt (FDS) (d) Results of the mass balance calculation for stage 2 represented in Table 4 for a sample from Neubulach (stage 2 of Fig. 9a) and from Freudenstadt (FDS) shown in Figs. 6 and 7. See text for discussion.

Figure 15

(a) Illustration of a typical weathering profile and element speciation through a hydrothermal vein including the assumed position of the different weathering stages 1-4 illustrated in (b). Elements which are originated from fahlore and are oxidized during weathering are bold.

Supplementary Fig. 1

Simplified geologic map and main tectonics of the sampled localities located in the Northern and Central Schwarzwald (modified after Villinger and Zedler, 2006).

Supplementary Fig. 2

Underground and hand specimen photos showing typical primary and weathering assemblages of the fahlore-rich mineralization. (a) Barite-fahlore vein cutting the Lower Triassic sandstone in the Neubulach visitor mine. Fahlore is still preserved and surrounded by several secondary minerals. (b) Hand specimen from Neubulach showing fahlore fractured by weathering stage 1 and surrounded by arsenates of weathering stage 2 (green). This is cut by younger azurite (blue with imprints of quartz crystals) of weathering stage 3. (c) Hand specimen from the Königswart mine showing abundant emplectite surround fahlore. The orange and green weathering assemblage is mostly found on fractures in quartz. (d) Hand specimen from the Dorothea mine near Freudenstadt showing fahlore with covellite of weathering stage 1.

Supplementary Fig. 3

(a) µXRD pattern of mixed phases of stage 3 from Königswart of Fig. 10. The Cu-arsenates and Cu-silicates cannot be identified and most likely represent the broad elevated background reflecting amorphous phases, whereas the intergrown barite of stage 4 is accountable for all reflexes. (b) and (c) µXRD pattern of stage 4 radial green minerals of a sample from Wittichen were identified as mixite (b) and malachite (c), both intergrown with quartz. (d) µXRD pattern of azurite from Neubulach.

Supplementary Fig. 4

Raman spectra of the Bi-poor and Bi-rich assemblage of stage 1 (Neubulach), the amorphous stage 2 phase of Fig. 6a (Freudenstadt), azurite (Neubulach), and mixite from Wittichen. Stage 2 phase and mixite show a water content with the broad peak at 3400-3500 cm^{-1} and the arsenate peak at 850 cm^{-1}.

Supplementary Fig. 5

(a) BSE image of stage 1 and 4 weathering assemblage (see also Fig. 1) before and after (inlet) the vacuum of the electron microprobe overnight. Cracks formed predominantly in bariopharmacosiderite. (b) BSE image of stage 2 and 4 weathering assemblage before the vacuum of the electron microprobe (see also Fig. 6). (c) SEI image of (b) after the vacuum of the electron microprobe overnight. Cracks formed mostly in the amorphous arsenate but also in tangdanite of stage 4.

Supplementary Fig. 6

Selected area diffraction patterns of (a) Fig. 3f of the Sb-Bi-bearing RGM, and (b) of Fig. 3g. of a mixture of Sb-Bi-bearing RGM with Cu-sulfides and the Cu-oxide phase.

Table

Table 1. *Representative TEM EDX results including the average compositions in wt.% and calculated apfu*

Stage	Number of analyses	Phase	Locality	Sample		As	Cu	Fe	Sb	Bi	S [wt.%]					
1	5	Cu-sulfide	Neubulach	JHa3	Average	0.5	80.4	0.7	0.6	1.1	16.8					
					±	0.5	1.2	0.4	0.6	2.4	3.2					
						As_2O_5	CuO	Fe_2O_3	Sb_2O_5	Bi_2O_3	SO_3 [wt.%]	SiO2	Al_2O_3	BaO	P_2O_5	
1	3	Cu-oxide phase	Neubulach	JHa3	Average	2.8	92.0	0.8	0.9	1.0	1.5	0.3	0.4	0.1	0.2	
					±	0.4	0.5	0.1	0.3	0.2	0.3	0.1	0.1	0.2	0.1	
1	5	Bi-Sb RGM	Neubulach	JHa3	Average	5.7	12.7	9.0	29.5	38.6	1.6	1.2	0.8	0.4	0.5	
					±	0.9	1.0	0.6	0.8	1.4	2.6	0.3	0.1	0.2	0.2	
3	6	Amorphous Cu-arsenate	Neubulach	JHa3	Average	13.0	65.5	2.9	2.3	4.7	10.0	0.6	0.6	0.1	0.4	
					±	2.2	9.7	1.1	0.8	1.6	7.0	0.7	0.3	0.2	0.3	
4	5	Amorphous Cu-arsenate, Bi-rich	Freudenstadt	MK65	Average	27.5	42.7	14.4	1.6	9.1	3.5	0.5	0.4	0.1	0.2	
					±	3.7	5.3	0.3	0.4	0.8	1.1	0.1	0.1	0.1	0.1	
4	4	Amorphous Cu-arsenate, Bi-poor	Freudenstadt	MK65	Average	17.0	28.5	8.8	2.0	3.7	28.6	6.8	2.0	1.5	1.1	
					±	5.5	4.6	0.6	1.6	2.9	14.2	0.4	0.3	0.1	0.3	

						As	Cu	Fe	Sb	Bi	S [apfu]					
1		Cu-sulfide	Neubulach	JHa3	Average	<0.1	2.5	<0.1	<0.1	<0.1	**1.0**					
					±	0.01	0.51	0.02	0.01	0.03	na					
						As	Cu	Fe	Sb	Bi	S [apfu]	Si	Al	Ba	P	Normalized to
1		Cu-oxide phase	Neubulach	JHa3	Average	<0.1	0.9	<0.1	<0.1	<0.1	<0.1	<0.1	<0.1	<0.1	<0.1	1.0	1 apfu O
					±		0.004	0.001	0.002	0.001	0.002	0.001	0.001	0.001	0.001		
1		Bi-Sb-bearing RGM	Neubulach	JHa3	Average	0.3	1.0	0.7	1.1	1.0	0.1	0.1	0.1	0.0	0.0	7.9	1 apfu Bi
					±	0.06	0.09	0.04	0.03		0.21	0.03	0.02	0.01	0.02	0.78	
3		Amorphous Cu-arsenate	Neubulach	JHa3	Average	4.0	29.4	1.3	0.5	0.7	4.4	0.4	0.4	0.0	0.2	58.7	100 at.%
					±	0.7	5.3	0.4	0.2	0.2	2.9	0.4	0.2	0.1	0.2	2.5	
4		Amorphous Cu-arsenate, Bi-rich	Freudenstadt	MK65	Average	8.8	19.7	6.6	0.4	1.4	1.6	0.3	0.3	<0.1	0.1	60.8	100 at.%
					±	1.1	2.6	0.1	0.1	0.1	0.5	0.1	0.1	<0.1	0.1	1.1	
4		Amorphous Cu-arsenate, Bi-poor	Freudenstadt	MK65	Average	4.3	10.3	3.1	0.4	0.5	9.9	3.2	1.1	0.3	0.4	66.5	100 at.%
					±	2.0	3.0	0.6	0.4	0.4	4.2	0.2	0.1	0.04	0.1	2.2	

Table 2. *Representative EMP results for sulfides including data in wt.% and calculated apfu for each analyses. b.d. = below detection limit*

Locality	Sample	Mineral	As	S	Bi	Cu	Pb	Hg	Ag	Zn	Sb	Fe	Ni	Co	Se	Total
									[wt.%]							
Neubulach	JHa3.4	Fahlore	16.3	27.3	0.14	42.1	b.d.	0.09	0.21	3.48	9.29	3.30	b.d.	0.04	0.06	99.6
Neubulach	JHa3.12	Fahlore	11.5	26.2	7.60	40.6	b.d.	0.07	0.25	3.73	6.75	2.71	b.d.	0.07	0.08	99.6
Freudenstadt	MK65.1	Fahlore	14.9	26.9	6.85	40.8	b.d.	b.d.	0.47	1.81	3.21	5.07	b.d.	0.36	0.05	100.5
Freudenstadt	MK65.3	Fahlore	16.1	27.9	0.14	41.8	b.d.	0.17	0.55	0.85	5.35	5.26	b.d.	0.43	0.02	99.5
Königswart	JHa4.25	Fahlore	11.7	25.8	12.8	40.2	b.d.	0.32	0.50	2.95	3.16	2.73	b.d.	0.11	0.06	100.5
Königswart	JHa4.19	Fahlore	13.8	27.4	0.11	41.7	b.d.	0.29	0.28	4.05	8.56	3.01	b.d.	0.06	0.07	99.4
Wittichen	JHa6.4	Fahlore	11.7	25.3	15.5	39.8	b.d.	0.48	0.29	5.16	0.65	1.15	b.d.	0.02	0.35	100.5
Wittichen	MK70.6	Fahlore	19.8	28.3	b.d.	43.2	b.d.	0.02	0.06	0.81	0.49	6.67	b.d.	b.d.	0.16	99.5
Wittichen	MK69.9	Chalcopyrite	0.07	34.5	0.05	33.3	b.d.	b.d.	0.14	b.d.	b.d.	31.0	b.d.	0.05	b.d.	99.1
Neubulach	MK63.1	Emplectite	b.d.	19.4	61.4	19.9	b.d.	b.d.	b.d.	0.03	0.26	b.d.	b.d.	b.d.	b.d.	100.9
Wittichen	MK66.16	Wittichenite	b.d.	19.2	41.5	38.8	b.d.	b.d.	0.13	b.d.	0.09	b.d.	b.d.	b.d.	b.d.	99.8
Freudenstadt	JHa12.12	Spionkopite	1.03	25.1	0.54	69.2	b.d.	0.08	1.13	b.d.	0.08	0.23	b.d.	0.02	0.04	97.7
Neubulach	MK66.21	Covellite	0.13	33.0	0.36	64.9	b.d.	b.d.	0.12	b.d.	0.08	0.04	b.d.	b.d.	b.d.	98.6
			As	S	Bi	Cu	Pb	Hg	Ag	Zn	Sb	Fe	Ni	Co	Se	Normalized to
									[apfu]							
Neubulach	JHa3.4	Fahlore	2.8	13.1	<0.1	10.2		<0.1	<0.1	0.8	1.2	0.9		<0.1	<0.1	29 apfu
Neubulach	JHa3.12	Fahlore	2.5	13.1	0.6	10.2		<0.1	<0.1	0.9	0.9	0.8		<0.1	<0.1	29 apfu
Freudenstadt	MK65.1	Fahlore	3.5	13.0	<0.1	10.0		<0.1	<0.1	0.4	0.5	1.5		0.1	<0.1	29 apfu
Freudenstadt	MK65.3	Fahlore	2.8	13.0	0.6	10.1		<0.1	<0.1	0.4	0.6	1.3		0.1	<0.1	29 apfu
Königswart	JHa4.25	Fahlore	2.5	13.1	1.0	10.3		<0.1	0.1	0.7	0.4	0.8		<0.1	<0.1	29 apfu
Königswart	JHa4.19	Fahlore	2.8	13.1	<0.1	10.1		<0.1	<0.1	1.0	1.1	0.8		<0.1	<0.1	29 apfu
Wittichen	JHa6.4	Fahlore	2.6	13.0	1.2	10.3		<0.1	<0.1	1.3	0.1	0.3		<0.1	0.1	29 apfu
Wittichen	MK70.6	Fahlore	3.9	13.0		10.0		<0.1	<0.1	0.2	0.1	1.8			<0.1	29 apfu
Wittichen	MK69.9	Chalcopyrite	<0.1	2.0	<0.1	1.0			<0.1			1.0		<0.1		4 apfu
Neubulach	MK63.1	Emplectite		2.0	1.0	1.0				<0.1	<0.1					4 apfu
Neubulach	MK66.16	Wittichenite		3.0	1.0	3.0			<0.1		<0.1					7 apfu
Freudenstadt	JHa12.12	Spionkopite	0.05	27.8	0.1	38.0		<0.1	0.4		0.1	0.1		<0.1	<0.1	67 apfu
Neubulach	MK66.21	Covellite	<0.1	1.0	<0.1	1.0			<0.1		<0.1	<0.1				2 apfu

Table 3. Representative LA-ICP-MS elemental concentrations in ppm. n.d. = not detected

Sample	Locality	Mineral	stage	P	V	Cr	Mn	Co	Ni	Zn	Ga	Ge	Se	Mo	Ag	Cd	In	Sn	Tl	Pb
JHA-3A	Neubulach	fahlore	0	10	0.3	1.3	1.9	461	1.4	40964	n.d.	0.4	n.d.	0.2	1289	306	4	0.3	0.04	3
JHA-3B	Neubulach	fahlore	0	19	0.1	0.1	n.d.	624	1.2	35566	0.01	0.1	11	0.2	1300	140	13	2	0.02	2
JHA-3C	Neubulach	Stage 1	1	239	6	2	51	32	2	5626	1	2	6	4	1864	435	17	0.4	0.01	73
JHA-3D	Neubulach	Stage 1	1	124	3	1	11	9	3	2657	0.3	2	9	1	2575	52	9	0.2	0.02	34
JHA-3E	Neubulach	azurite	4	51	n.d.	0.03	0.2	5	5	273	n.d.	0.03	n.d.	0.05	0.4	n.d.	0.002	0.1	0.03	0.2
JHA-3F	Neubulach	Bi-Sb RGM	3	687	14	10	330	6	2	4077	0.3	8	7	8	2645	1181	37	0.1	0.05	275
JHA-3G	Neubulach	Bi-Sb RGM	3	332	8	9	195	5	1	2678	0.2	4	4	4	1627	662	23	1	0.004	152
JHA-3I	Neubulach	Stage 1	1	152	3	0.5	130	17	1	3458	n.d.	1	5	1	3750	122	14	0.2	n.d.	9
JHA-3J	Neubulach	Bi-Sb RGM	3	382	10	6	194	4	1	2666	0.2	4	12	4	2195	720	29	0.3	0.02	61
JHA-3K	Neubulach	Bi-Sb RGM	3	314	7	3	134	5	1	2559	0.2	2	4	5	1962	494	23	1	n.d.	52
JHA-3L	Neubulach	Bi-Sb RGM	3	337	7	3	182	4	1	2705	0.2	4	4	4	2303	685	22	0.4	n.d.	67
JHA-7A	Königswart	fahlore	0	29	0.1	2.1	0.2	1212	3	46233	0.3	0.4	30	0.2	4333	167	7	n.d.	0.1	4
JHA-7B	Königswart	Amorphous Cu-arsenates	2	892	0.2	0.2	1	71	1	4774	n.d.	0.4	13	1	2321	48	7	0.3	0.03	7
JHA-7C	Königswart	Amorphous Cu-silicate II	3	776	4	8	3	14	1	2658	0.2	4	n.d.	2	2	26	0.03	0.2	0.1	104
JHA-7D	Königswart	chalcopyrite	0	82	0.1	0.01	0.2	n.d.	0.4	8	n.d.	2	n.d.	0.1	517	n.d.	1	1	n.d.	0.4
JHA-7E	Königswart	Cu-Fe-oxide	1	391	n.d.	0.1	1	8	22	2984	n.d.	4	7	6	64	27	2	4	n.d.	11
JHA-7F	Königswart	mixite	4	379	8	0.01	3	25	26	4952	0.3	0.2	38	34	1	244	1	0.1	0.01	2850
MK-65-B	Freudenstadt	fahlore		72	n.d.	0.5	0.5	3109	1	28511	0.4	0.1	7	42	2220	141	30	n.d.	0.1	58
MK-65-C	Freudenstadt	fahlore	0	158	0.2	0.2	0.8	1345	1	18982	0.1	1	n.d.	19	8324	104	43	0.3	0.03	26
MK-65-D	Freudenstadt	Amorphous Cu-arsenates	2	341	0.2	1	2	215	0.4	3245	0.3	0.2	n.d.	6	7855	40	85	1	0.01	38
MK-65-E	Freudenstadt	Amorphous Cu-arsenates	2	335	0.1	0.3	1	245	n.d.	3367	0.3	0.3	3	7	9326	45	95	2	0.02	33
MK-65-F	Freudenstadt	tangdanite	4	141	0.4	2	1	138	n.d.	3708	1	n.d.	14	19	24	27	0.04	0.2	0.003	1
MK-68-A	Wittichen	mixite	4	217	8	0.4	262	99	1057	72	0.2	n.d.	9	7	0.1	38	n.d.	0.2	0.04	127
MK-68-B	Wittichen	atelestite	4	569	465	0.1	6	10	17	159	0.03	0.4	2	143	5	4	0.1	0.1	1	399
MS-4A	Neubulach	azurite	4	502	1	1	2	4	0.2	714	0.1	0.01	n.d.	0.03	10	4	5	0.3	n.d.	4

MS-4B	Neubulach	Amorphous Cu-arsenates	2	275	2	0.1	14	60	1	10535	0.1	1	n.d.	1	56	149	23	0.1	0.1	31
MS-4C	Neubulach	fahlore	0	30	0.1		1.9	1192	2.4	59422	n.d.	0.3	18	0.8	936	349	11	n.d.	0.3	28
MS-4D	Neubulach	fahlore	0	462	1.5	2.0	47.3	777	1.4	41861	1	0.5	n.d.	0.4	1184	215	17	1	0.2	9
MS-4E	Neubulach	Stage 1	1	1144	2	5	50	45	1	3797	0.01	0.4	n.d.	0.2	1520	40	13	0.2	0.03	6
MS-4F	Neubulach	Stage 1	1	819	11	15	88	117	7	6944	2	6	60	9	1359	2260	38	n.d.	0.1	85

Table 4. *Representative EMP results for minerals of stage 1-4 including wt.% and calculated mol% and atoms per formula unit (apfu) for each analysis. b.d. = below detection limit*

Stage	Phase	Locality	Sample	As_2O_3	SO_3	Bi_2O_3	CuO	Al_2O_3	PbO	HgO	Ce_2O_3 [wt.%]	Ag2O	ZnO	Sb_2O_3	Fe_2O_3	CaO	BaO	SiO_2	Theor. H_2O	Theor. CO_2	Total
2	Amorphous Cu-arsenates	Neubulach	JHa3.s18	21.0	0.69	12.3	39.6	b.d.	b.d.	b.d.	0.04	0.20	1.15	3.77	4.56	1.41	0.95	0.19			85.78
2	Amorphous Cu-arsenates	Freudenstadt	MK65.s34	26.4	0.95	1.41	41.8	0.06	b.d.	b.d.	b.d.	0.36	0.14	1.95	11.8	0.14	0.12	0.07			85.17
2	Amorphous Cu-arsenates	Freudenstadt	MK65.s32	23.2	0.69	9.64	39.2	b.d.	b.d.	b.d.	b.d.	0.07	0.16	3.77	9.32	0.08	0.09	0.14			86.44
2	Amorphous Cu-arsenates	Freudenstadt	JHa12.s15	38.1	b.d.	1.15	50.1	0.15	b.d.	b.d.	b.d.	b.d.	0.68	1.41	1.33	0.15	0.13	0.03			93.18
2	Amorphous Cu-arsenates	Königswart	JHa4.s17	21.5	1.29	12.5	31.2	0.08	b.d.	0.09	b.d.	b.d.	0.68	2.85	10.9	1.26	2.76	1.10			86.22
3	Amorphous Cu-silicate I	Königswart	JHa7.s13	6.35	0.98	4.14	49.0	0.06	b.d.	0.30	b.d.	0.39	0.36	1.61	2.35	0.60	0.62	22.6			89.33
3	Amorphous Cu-silicate II	Königswart	JHa7.s14	5.05	b.d.	1.84	52.9	0.05	b.d.	b.d.	b.d.	b.d.	0.21	1.27	0.08	0.19	0.11	11.9			73.57
4	Azurite	Neubulach	JHa3.s3	b.d.	b.d.	b.d.	63.4	0.04	b.d.	b.d.	b.d.	b.d.	b.d.	b.d.	b.d.	0.06	0.10	b.d.	5.2	25.5	63.54
4	Malachite	Neubulach	MK66.s3	1.74	b.d.	b.d.	63.8	0.10	b.d.	b.d.	b.d.	0.04	0.28	0.03	0.03	0.08	0.10	0.03	8.2	19.9	66.25
4	Malachite	Freudenstadt	MK65.s3	0.80	b.d.	b.d.	64.7	b.d.	b.d.	0.12	b.d.	b.d.	0.25	0.40	b.d.	b.d.	0.14	0.05	8.2	19.9	66.45
4	Malachite	Königswart	JHa4.s9	1.37	b.d.	b.d.	61.8	b.d.	b.d.	b.d.	b.d.	b.d.	2.67	0.20	b.d.	b.d.	0.12	0.09	8.2	19.9	66.28
4	Malachite	Wittichen	MK70.s8	2.54	0.38	3.79	60.38	0.03	b.d.	b.d.	b.d.	b.d.	0.22	0.09	0.21	0.08	0.13	0.22	8.2	19.9	68.06
4	Mixite-group (mixite)	Wittichen	MK68.s2	30.3	b.d.	15.5	40.9	0.04	b.d.	b.d.	b.d.	b.d.	b.d.	b.d.	0.13	1.55	0.09	0.08	9.3		88.55
4	Mixite-group (zalesiite)	Neubulach	JHa3.s1	31.5	b.d.	7.04	43.6	0.16	b.d.	b.d.	b.d.	b.d.	0.05	b.d.	0.02	5.06	0.10	0.09	11.7		87.58
4	Mixite-group (zalesiite)	Königswart	Jha7.s28	30.7	b.d.	6.56	42.0	0.08	0.19	b.d.	b.d.	b.d.	0.24	b.d.	0.24	4.61	0.11	0.07	11.7		84.82
4	Barite	Königswart	JHa7.s20	b.d.	34.2	b.d.	0.10	0.89	b.d.	b.d.	0.08	b.d.	b.d.	b.d.	0.03	0.02	63.4	b.d.			98.71
4	Atelestite	Wittichen	MK68.s4	17.5	b.d.	70.8	0.25	b.d.	b.d.	b.d.	b.d.	b.d.	b.d.	0.05	b.d.	0.48	0.16	0.35	2.0		89.66
4	Olivenite	Freudenstadt	MK65.s28	38.3	0.46	b.d.	53.2	0.06	b.d.	b.d.	b.d.	0.03	0.31	1.71	0.05	0.02	0.14	b.d.	3.2		94.31
4	Cornubite/Cornwallite	Freudenstadt	MK65.s5	27.4	0.79	b.d.	52.8	0.08	b.d.	b.d.	b.d.	b.d.	0.60	2.78	0.32	0.17	0.13	0.53	7.9		85.58
4	Dussertite/ arsenogorceixite	Freudenstadt	MK65.s13	28.84	0.17	1.08	1.49	7.46	b.d.	0.09	b.d.	0.03	0.38	13.99	15.23	0.31	18.79	b.d.	6.7-9.9		87.85
4	Tangdanite	Freudenstadt	MK65.s1	30.0	2.36	b.d.	46.8	0.05	b.d.	b.d.	b.d.	b.d.	0.19	0.19	0.04	7.80	0.18	0.15	15.5		87.76
4	Clinoclase	Königswart	JHa4.s8	25.5	b.d.	0.24	55.0	b.d.	b.d.	b.d.	b.d.	b.d.	1.86	0.69	b.d.	0.09	0.12	0.15	7.1		83.63

	Phase	Locality	Sample	As_2O_3	SO_3	Bi_2O_3	CuO	Al_2O_3	PbO	HgO	Ce_2O_3 [mol %]	Ag2O	ZnO	Sb_2O_3	Fe_2O_3	CaO	BaO	SiO_2	Normalized to

2	Amorphous Cu-arsenates	Neubulach	JHa3.s18	12.2	1.2	3.5	66.5	0			<0.1	0.1	1.9	1.6	8.5	3.4	0.8	0.4	mol %
2	Amorphous Cu-arsenates	Freudenstadt	MK65.s34	13.8	1.4	0.4	63.0	<0.1				0.2	0.2	0.7	19.7	0.3	0.1	0.1	mol %*
2	Amorphous Cu-arsenates	Freudenstadt	MK65.s32	13.1	1.1	2.7	63.9					<0.1	0.7	1.5	16.8	0.2	0.1	0.3	mol %*
2	Amorphous Cu-arsenates	Freudenstadt	JHa12.s15	19.9		0.3	75.4	0.2				0	1.0	0.5	2.2	0.3	0.1	<0.1	mol %*
2	Amorphous Cu-arsenates	Königswart	JHa4.s17	12.3	2.1	3.6	51.8	0.1		0.1		0	1.1	1.2	20.0	3.0	2.4	2.4	mol %*
3	Amorphous Cu-silicate I	Königswart	JHa7.s13	2.5	1.1	0.8	55.9	0.1		0.1		0.1	0.40	0.45	3.0	1.0	0.4	34.2	mol %*
3	Amorphous Cu-silicate II	Königswart	JHa7.s14	2.4		0.4	73.8	0.1					0.3	0.4	0.1	0.4	0.1	21.9	mol %*
				As	**S**	**Bi**	**Cu**	**A**	**Pb**	**Hg**	**Ce [apfu]**	**Ag**	**Zn**	**Sb**	**Fe**	**Ca**	**Ba**	**Si**	
4	Azurite	Neubulach	JHa3.s3				3.0	<0.1								<0.1	<0.1		3 apfu Cu
4	Azurite	Freudenstadt	MK65.s14	0.1	0.3		3.0	<0.1				<0.1		<0.1	<0.1		<0.1		3 apfu Cu
4	Malachite	Neubulach	MK66.s3	<0.1			2.0	<0.1				<0.1	<0.1	<0.1	<0.1	<0.1	<0.1	<0.1	2 apfu Cu
4	Malachite	Freudenstadt	MK65.s3	<0.1			2.0			>0.1		>0.1	>0.1				>0.1	>0.1	2 apfu Cu
4	Malachite	Königswart	JHa4.s9	<0.1			2.0						0.1	<0.1			<0.1	<0.1	2 apfu Cu
4	Malachite	Wittichen	MK70.s8	0.1	<0.1	<0.1	2.0	<0.1					<0.1	<0.1	<0.1	<0.1	<0.1	<0.1	2 apfu Cu
4	Mixite-group (mixite)	Wittichen	MK68.s2	3.0		0.8	5.9	<0.1							<0.1	0.3	<0.1	<0.1	10 apfu cations
4	Mixite-group (zalesiite)	Neubulach	JHa3.s1	2.9		0.3	5.8	<0.1					<0.1		<0.1	1.0	<0.1	<0.1	10 apfu cations
4	Mixite-group (zalesiite)	Königswart	Jha7.s28	2.9		0.3	5.8	<0.1	<0.1				<0.1		<0.1	0.9	<0.1	<0.1	10 apfu cations
4	Barite	Königswart	JHa7.s20		1.0		<0.1	<0.1			<0.1				<0.1	<0.1	1.0		1 apfu Ba
4	Atelestite	Wittichen	MK68.s4	1.0		2.0	<0.1							<0.1		<0.1	<0.1	<0.1	2 apfu Bi
4	Olivenite	Freudenstadt	MK65.s28	1.0	<0.1		2.0	<0.1				<0.1	<0.1	<0.1	<0.1	<0.1	<0.1		2 apfu Cu
4	Cornubite/Cornwallite	Freudenstadt	MK65.s5	1.8	<0.1		5.0	<0.1					<0.1	<0.1	<0.1	<0.1	<0.1	<0.1	5 apfu Cu
4	Dussertite/ arsenogorceixite	Freudenstadt	MK65.s13	2.0	<0.1	<0.1	0.1	1.2		<0.1		<0.1	<0.1	0.7	1.7	<0.1	1.0		2 apfu As
4	Tangdanite	Freudenstadt	MK65.s1	3.8	0.4		8.5	<0.1					<0.1	<0.1	<0.1	2	<0.1	<0.1	2 apfu Ca
4	Clinoclase	Königswart	JHa4.s8	1.0		<0.1	3.0						0.1	<0.1		<0.1	<0.1	<0.1	3 apfu Cu

Table 5. Mass balance calculation for stage 1 and 2 weathering displayed in Fig. 14. See text for calculation and discussion.

	Neubulach, JHa3, Bi-rich	**Neubulach, JHa3, Bi-poor**	**Neubulach, MK63, Bi-rich**	**Freudenstadt, JHa12, medium Bi**	**Neubulach all fahlore**	**Neubulach high Bi fahlore**	**FDS dark zone (Fig. 5a, b-c)**	**FDS bright zone (Fig. 5a, d-f)**	**Königswart**	**Wittichen (Alte Gabe Gottes)**
	stage 1						stage 2			
average fahlore analyses	n=6 fahlore	n=9 fahlore	n=8 fahlore	n=8 fahlore	n=18 fahlore	n=9 fahlore	n=10 fahlore	n=10 fahlore	n=19 fahlore	n=11 fahlore
Average secondary assemblage	n=12 graphics	n=7 graphics	n=7 graphics	n=3 graphics	n=3 sek	n=3 sek	n=4 sek	n=3 sek	n=8 sek	n=4 sek
Cu [%]	43	28	43	43	-28	-27	-29	-29	-49	-25
Fe [%]	-19	-55	-2	-61	21	29	55	48	112	50
Zn [%]	-100	-94	-100	-100	-83	-82	-92	-93	-84	-75
As [%]	-83	-85	-83	-86	5	17	-5	11	-5	10
Sb [%]	-10	-56	-5	-14	-69	-62	-68	-36	-39	-65
Bi [%]	-12	-2	-22	0	101	11	76	-7	-3	-24
S [%]	-67	-80	-76	-83	-98	-98	-99	-99	-97	-99

***Table 6**. Comparison of the different weathering stages*

		Stage 1	Stage 2	Stage 3	Stage 4
Mineralogy of weathering products		Oxides Sulfides (Cu sulfides, acanthite, cinnabar)	No oxides Minor sulfate (barite), minor amounts of sulfides (acanthite, cinnabar)	No oxides No sulfide or sulphate	No oxides Sulfate (barite)
		No arsenate	arsenate	arsenate	arsenate
Crystallinity of secondary phases		Nano-meter to micro- meter sized crystals	Amorphous, local nano meter-sized crystals	Amorphous and botryoidal textures	Up to cm large crystals
Chemistry of secondary phases	Hydrous phases present	No hydrous phases	Hydrous phases	No hydrous phases	Hydrous phases
	Addition of elements	Si, Cu	Ba, Fe	Si	local Ca, Si, Ba, Al, and/or C
	Loss of elements	As, Zn, S, (Fe and Sb if fahlore is Bi-poor)	S, Zn, Sb, Cu	Not investigated	Not investigated
	Immobile elements	Bi (Fe and Sb if fahlore contains Bi)	Bi, As	Not investigated	Not investigated
Location of weathering products		Replaces fahlore	Replaces fahlore	Replaces older weathering phases	Spatially not related to fahlore, partly replaces older weathering phases
Weathering texture		Finger-like tubes forming 3D network through fahlore crystallizing from a gel-like precursor phase	Weathering assemblage forms fronts through fahlore, partly alternating phases, layers with nm-sized porosity	Weathering assemblage forms fronts through older weathering phases and/or cements them	Secondary minerals sealing cracks, local replacement of older weathering phases

Figure1

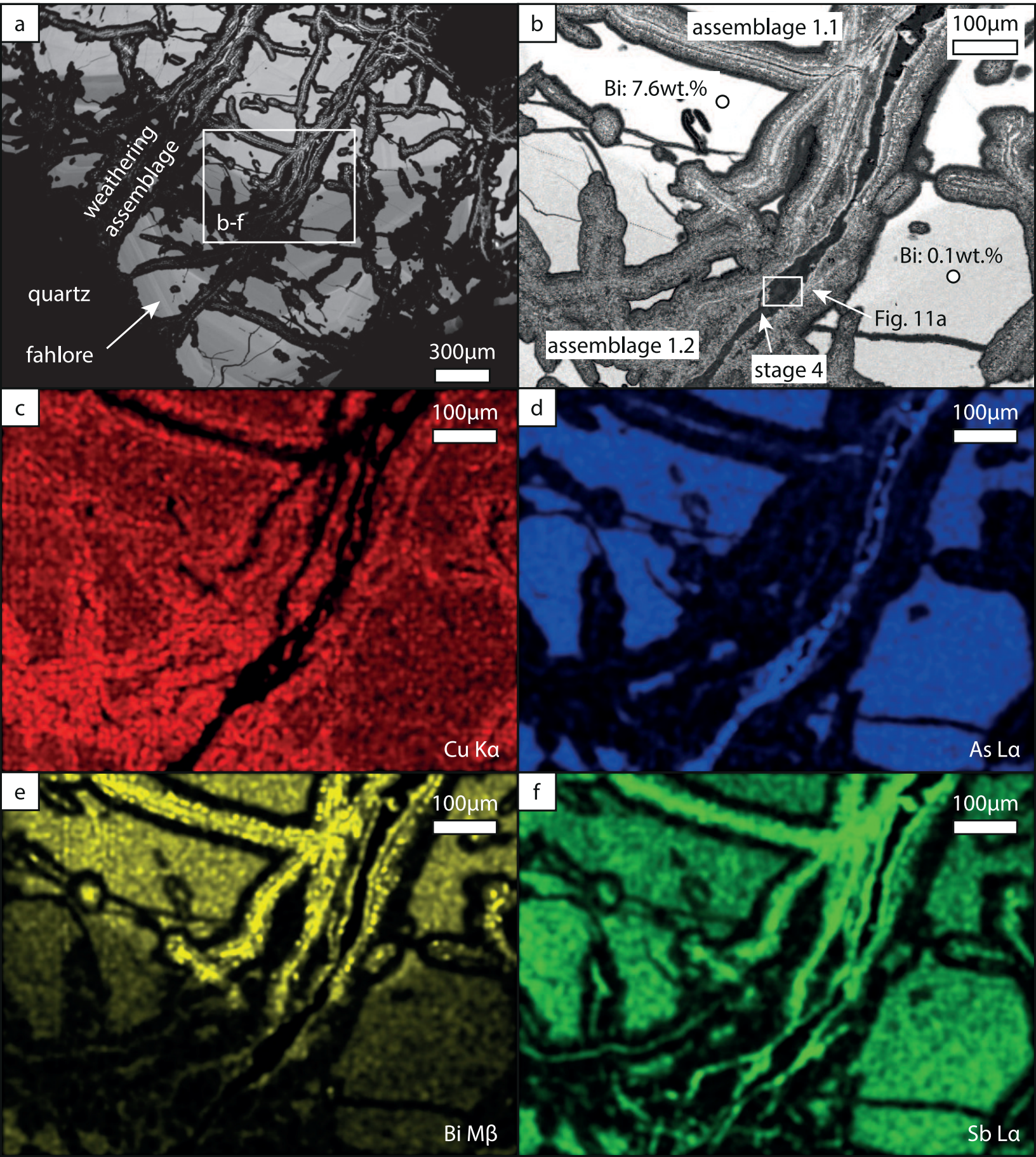
a
weathering assemblage
b-f
quartz
fahlore
300µm
b
assemblage 1.1
100µm
Bi: 7.6wt.%
Bi: 0.1wt.%
Fig. 11a
assemblage 1.2
stage 4
c
100µm
Cu Kα
d
100µm
As Lα
e
100µm
Bi Mβ
f
100µm
Sb Lα

Figure2

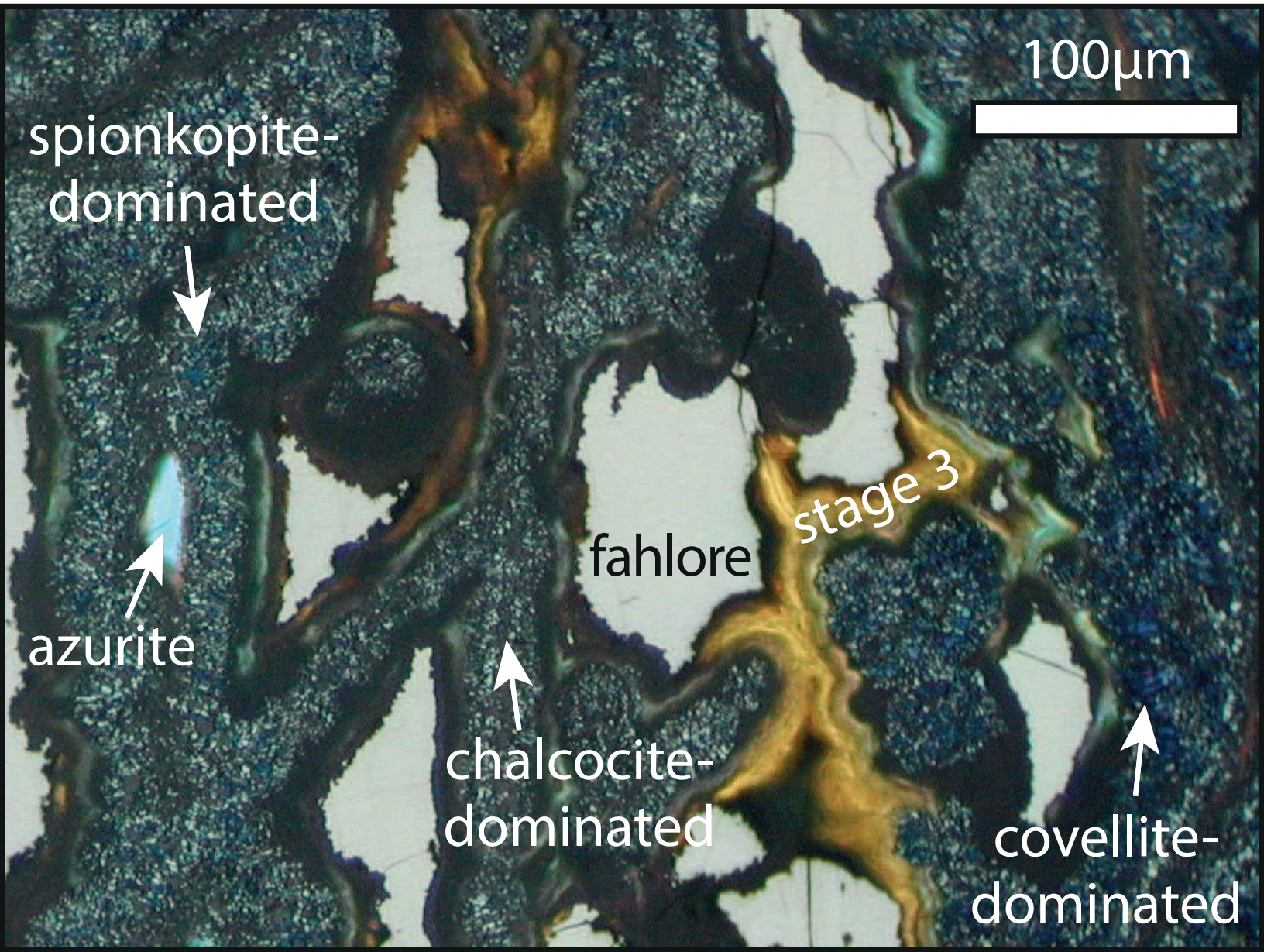
100µm
spionkopite-
dominated
azurite
fahlore
stage 3
chalcocite-
dominated
covellite-
dominated

Figure3

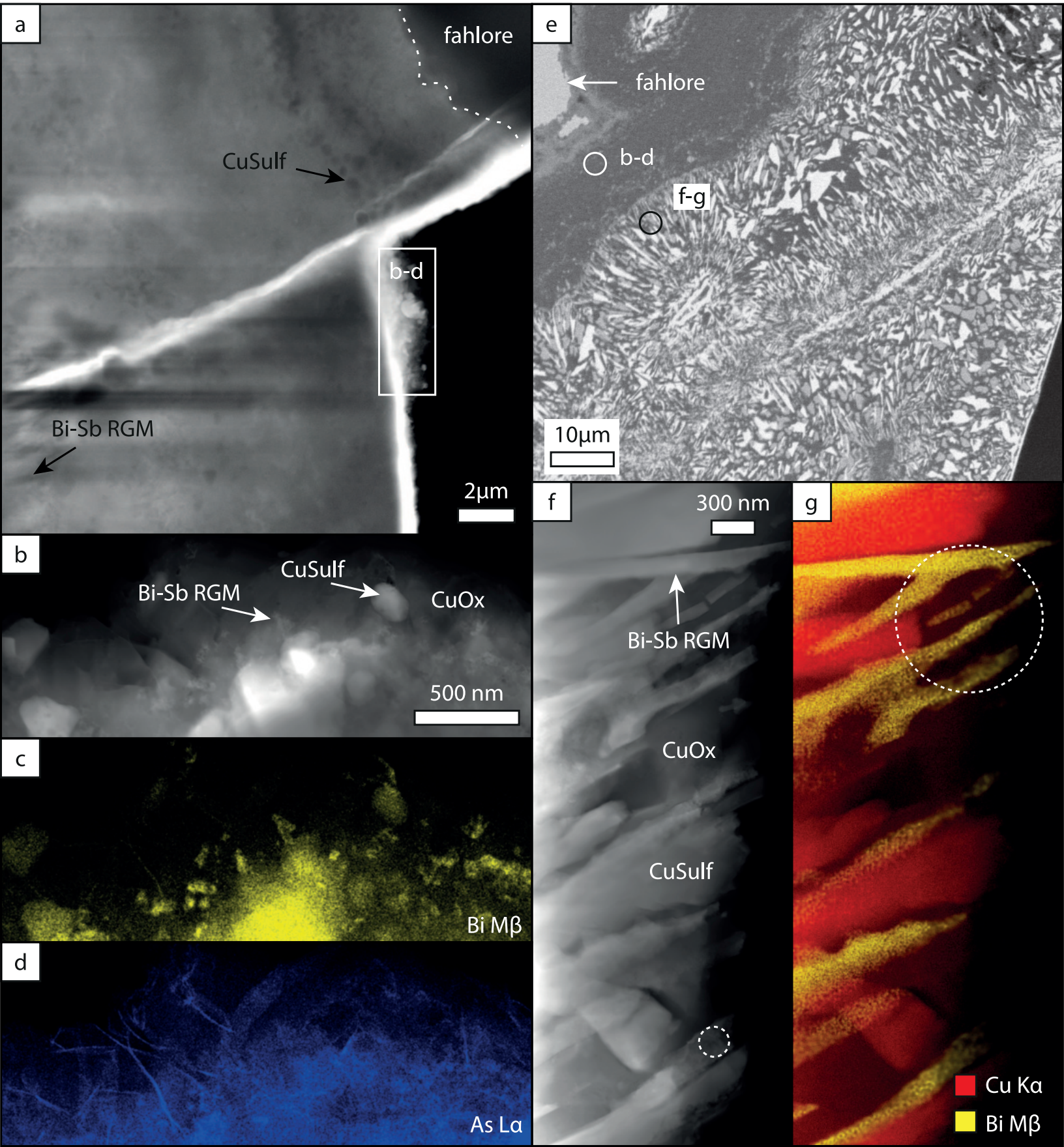
a
fahlore
CuSulf
b-d
Bi-Sb RGM
2µm
b
Bi-Sb RGM
CuSulf
CuOx
500 nm
c
Bi Mβ
d
As Lα
e
fahlore
b-d
f-g
10µm
f
300 nm
Bi-Sb RGM
CuOx
CuSulf
g
Cu Kα
Bi Mβ

Figure4

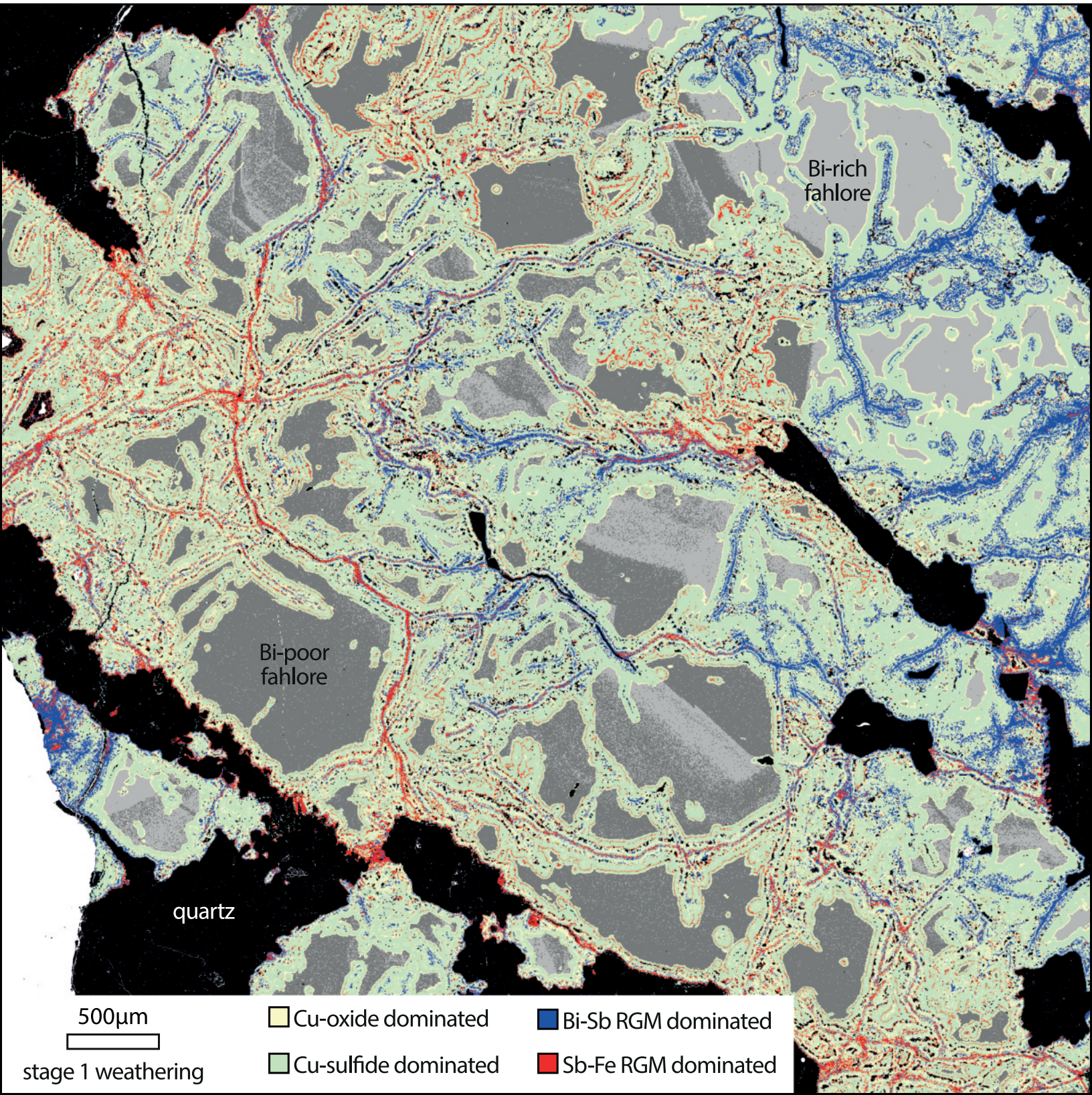
Bi-rich
fahlore
Bi-poor
fahlore
quartz
500µm
stage 1 weathering
Cu-oxide dominated
Cu-sulfide dominated
Bi-Sb RGM dominated
Sb-Fe RGM dominated

Figure5

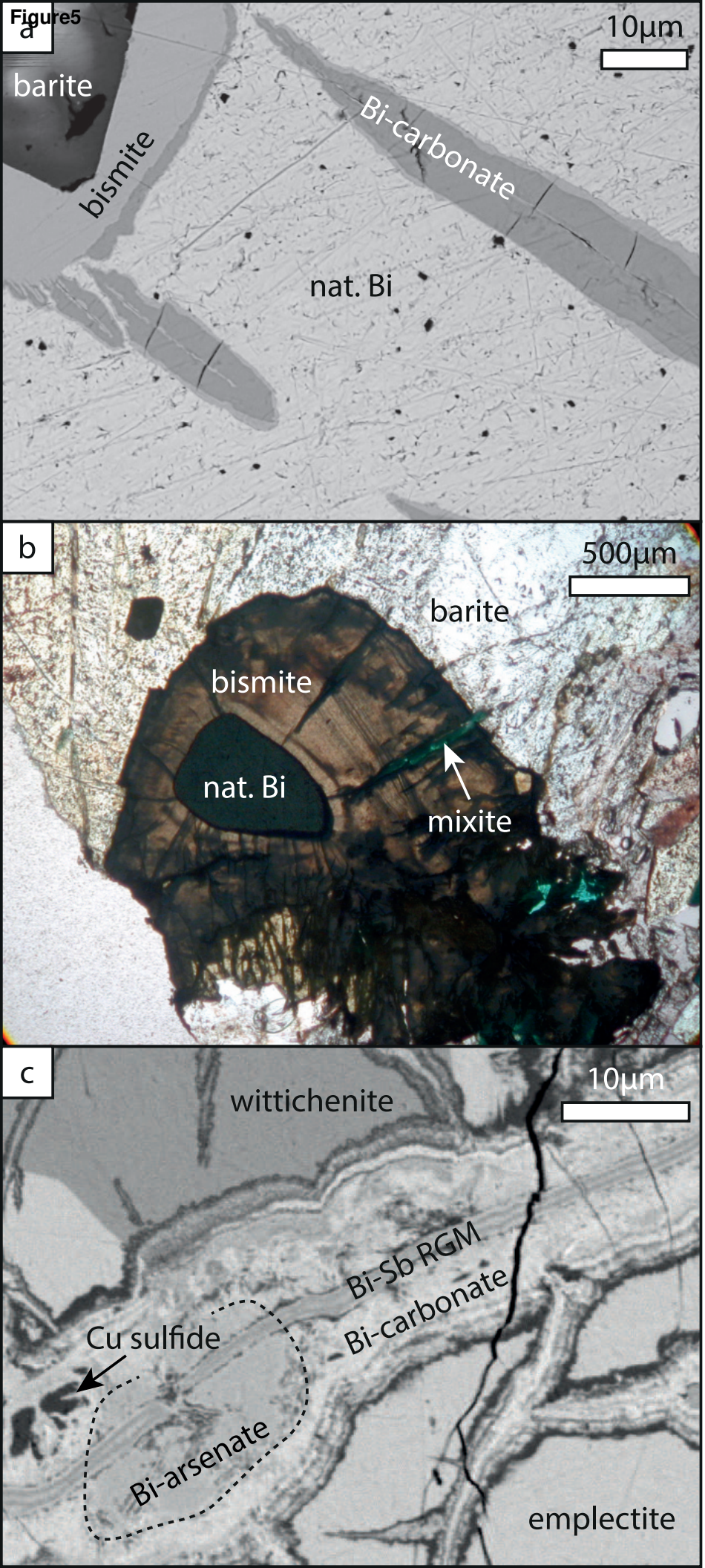
a
10µm
barite
bismite
Bi-carbonate
nat. Bi
b
500µm
barite
bismite
nat. Bi
mixite
c
10µm
wittichenite
Bi-Sb RGM
Bi-carbonate
Cu sulfide
Bi-arsenate
emplectite

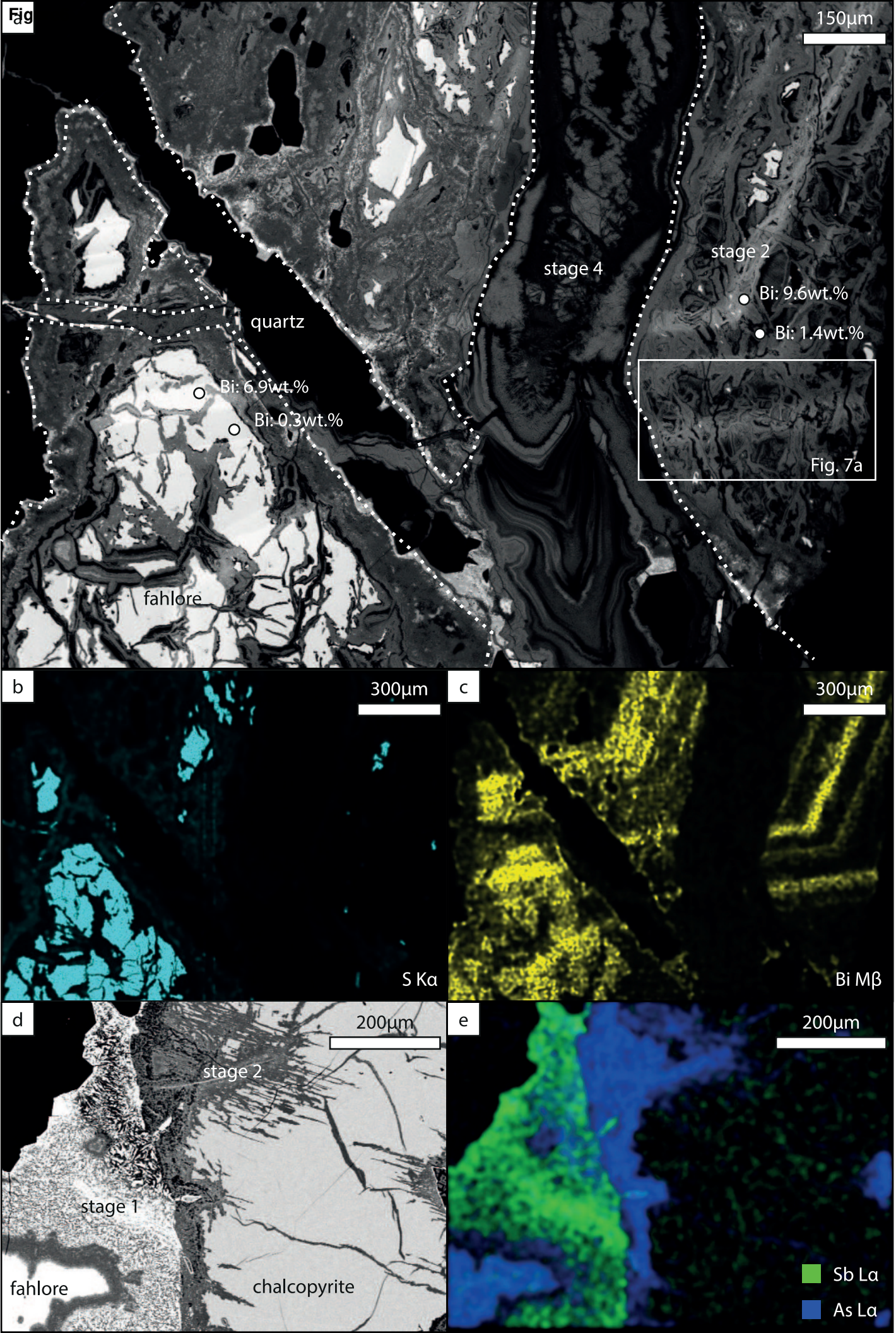
a
150µm
stage 4
stage 2
Bi: 9.6wt.%
Bi: 1.4wt.%
quartz
Bi: 6.9wt.%
Bi: 0.3wt.%
Fig. 7a
fahlore
b
300µm
S Kα
c
300µm
Bi Mβ
d
200µm
stage 2
stage 1
fahlore
chalcopyrite
e
200µm
Sb Lα
As Lα

Figure7

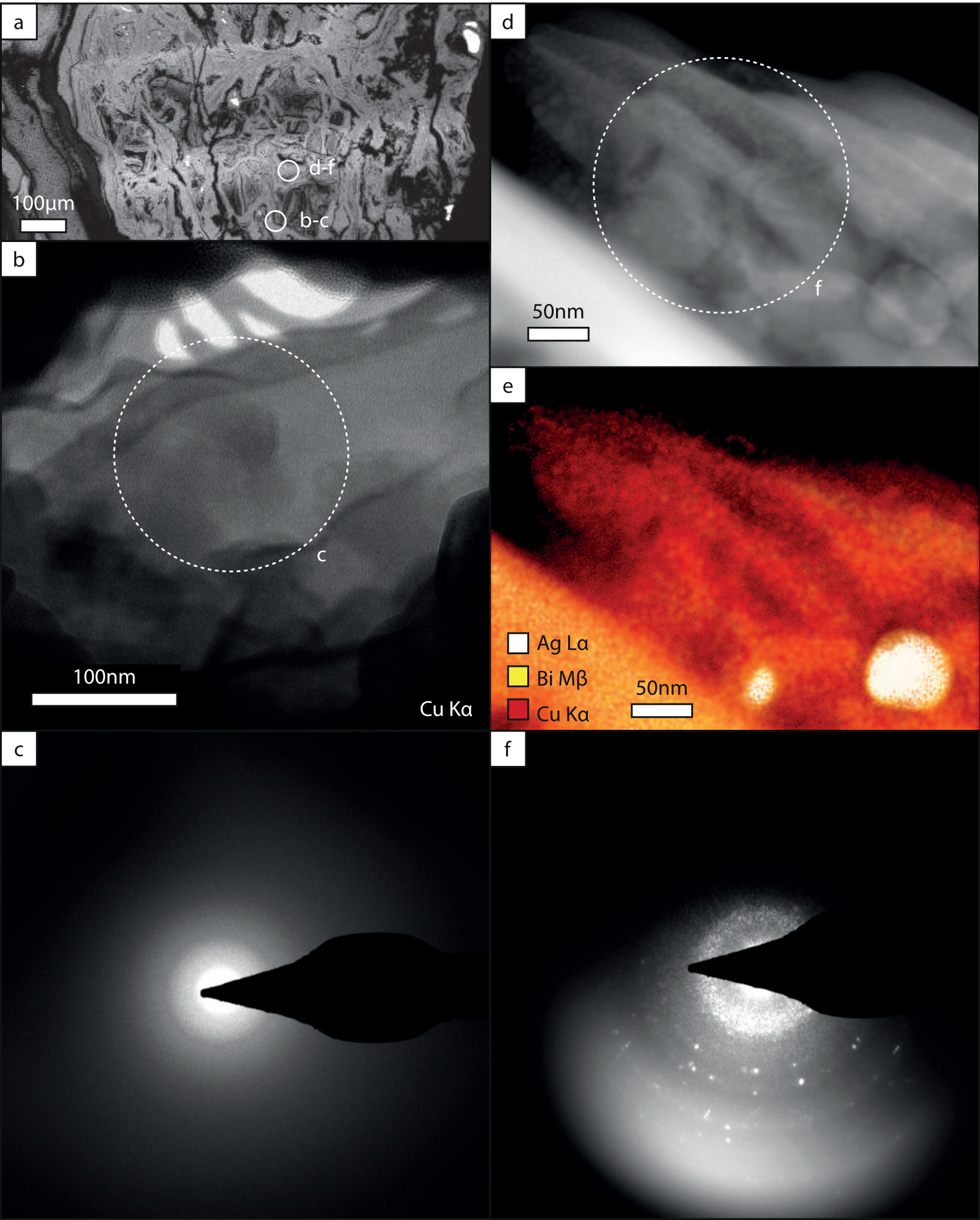

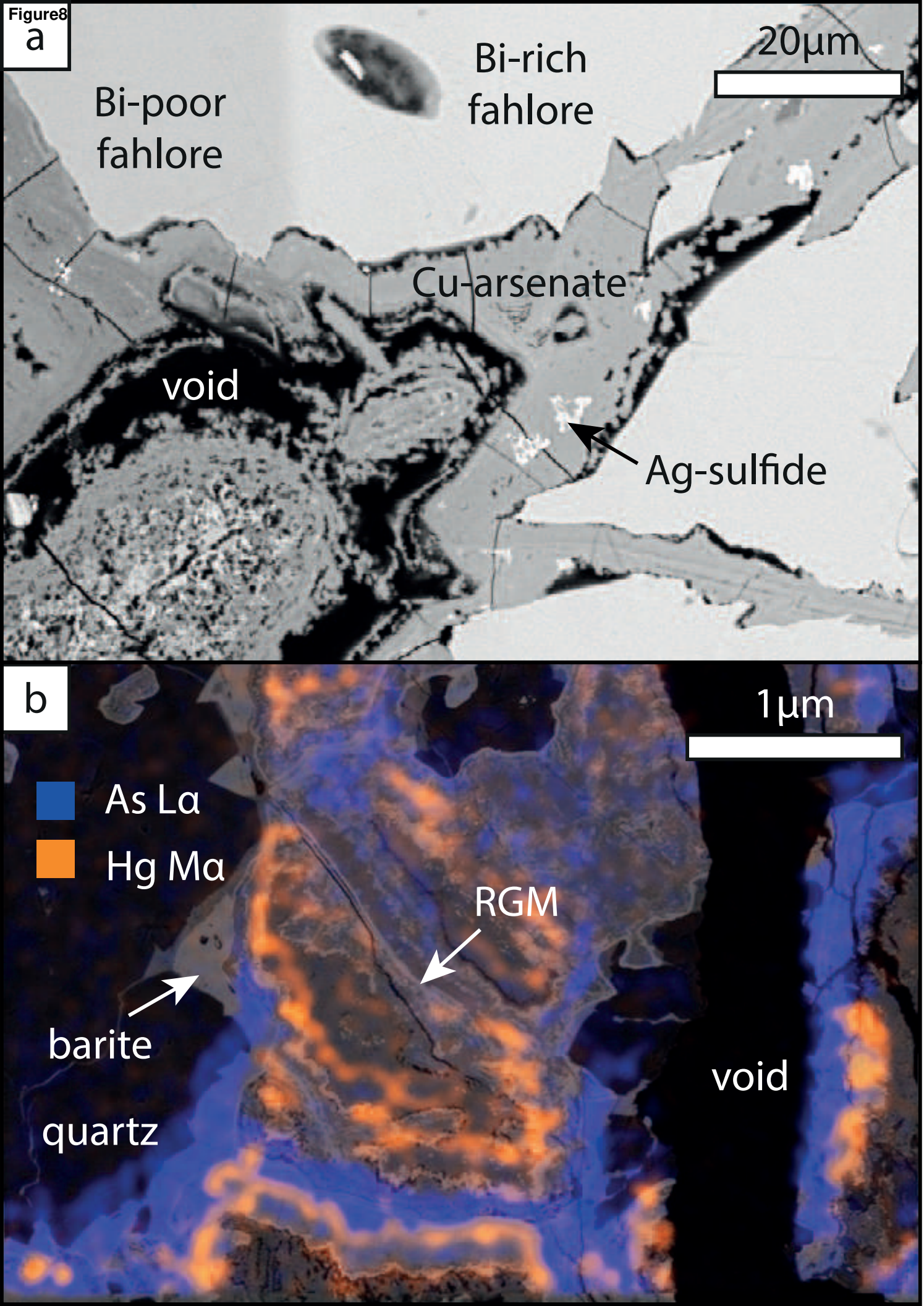
Figure8
a
Bi-poor
fahlore
Bi-rich
fahlore
20µm
Cu-arsenate
void
Ag-sulfide
b
1µm
As Lα
Hg Mα
RGM
barite
quartz
void

Figure9

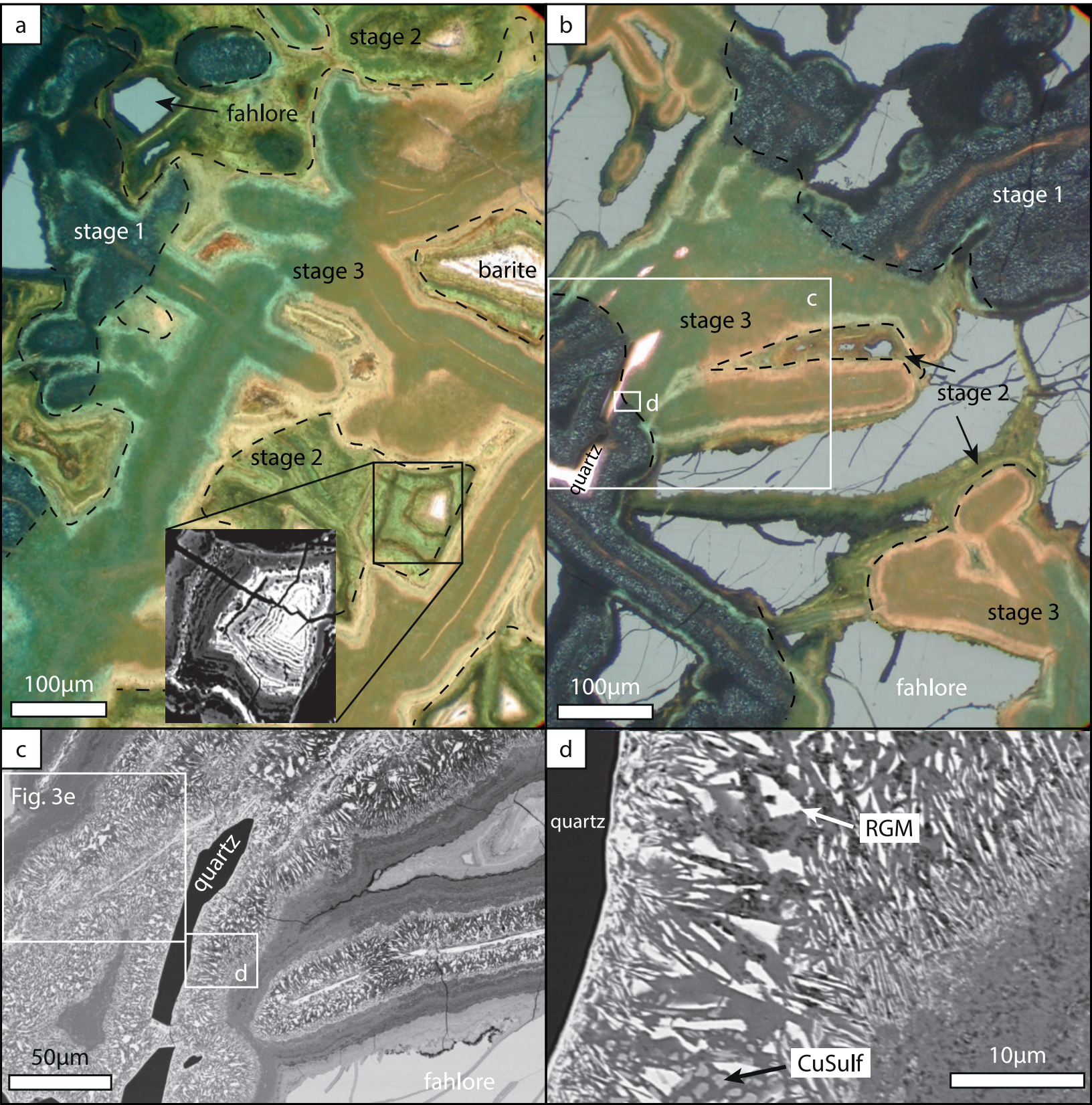
a
stage 2
fahlore
stage 1
stage 3
barite
stage 2
100µm
b
stage 1
c
stage 3
d
stage 2
quartz
stage 3
100µm
fahlore
c
Fig. 3e
quartz
d
50µm
fahlore
d
quartz
RGM
CuSulf
10µm

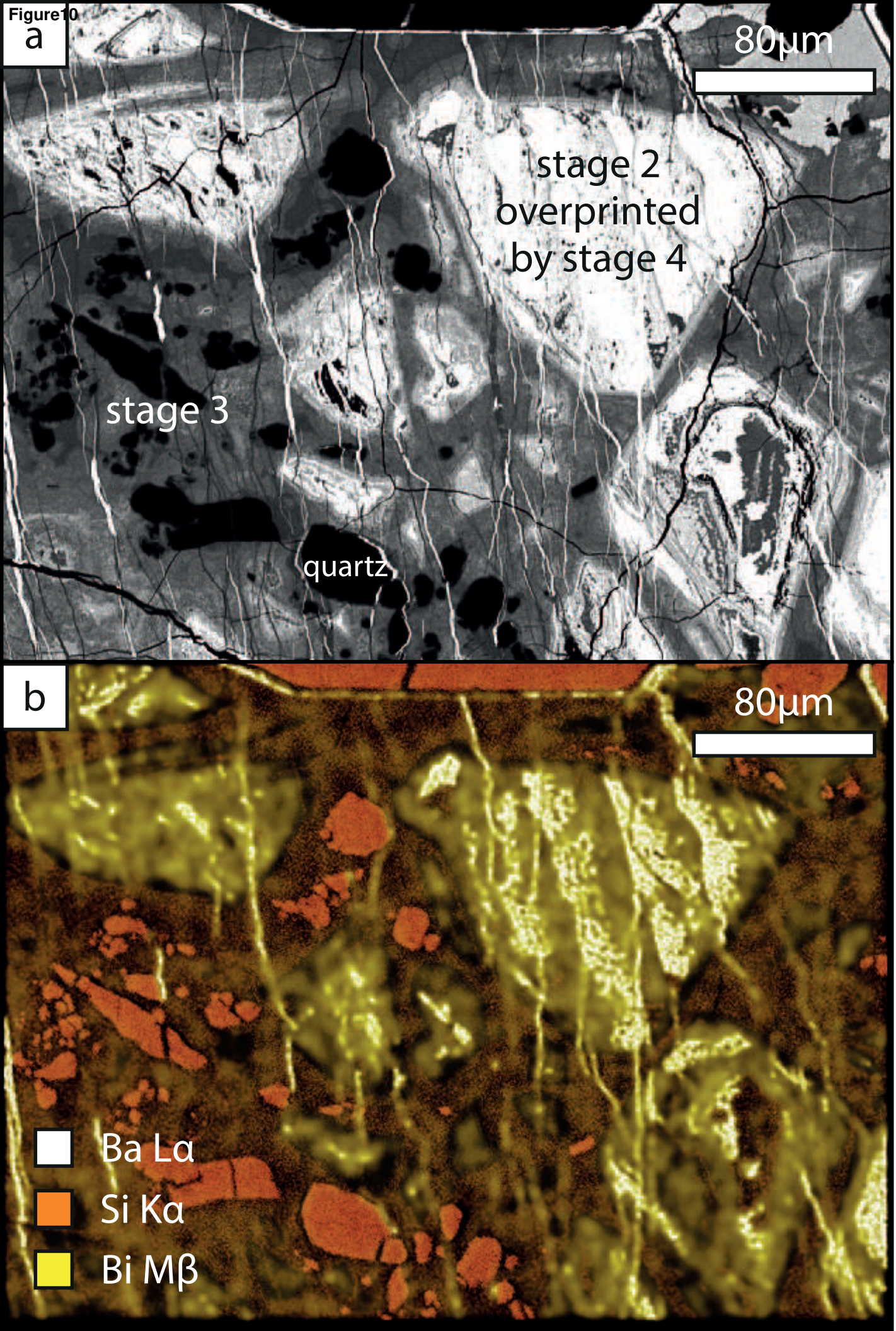
Figure10
a
80µm
stage 2
overprinted
by stage 4
stage 3
quartz
b
80µm
Ba Lα
Si Kα
Bi Mβ

Figure11

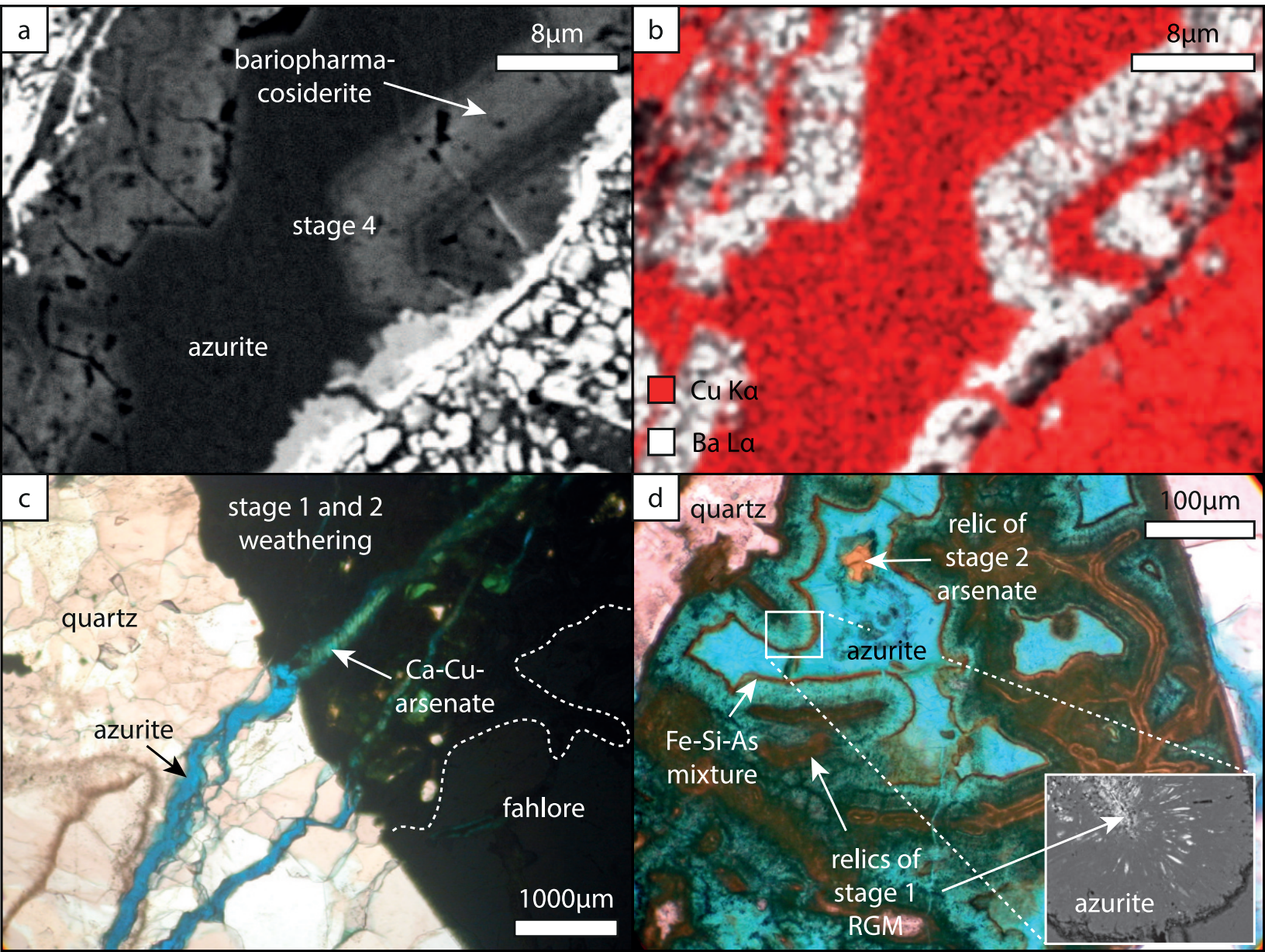
a
8µm
bariopharma-
cosiderite
stage 4
azurite
b
8µm
Cu Kα
Ba Lα
c
stage 1 and 2
weathering
quartz
Ca-Cu-
arsenate
azurite
fahlore
1000µm
d
quartz
100µm
relic of
stage 2
arsenate
azurite
Fe-Si-As
mixture
relics of
stage 1
RGM
azurite

Figure12

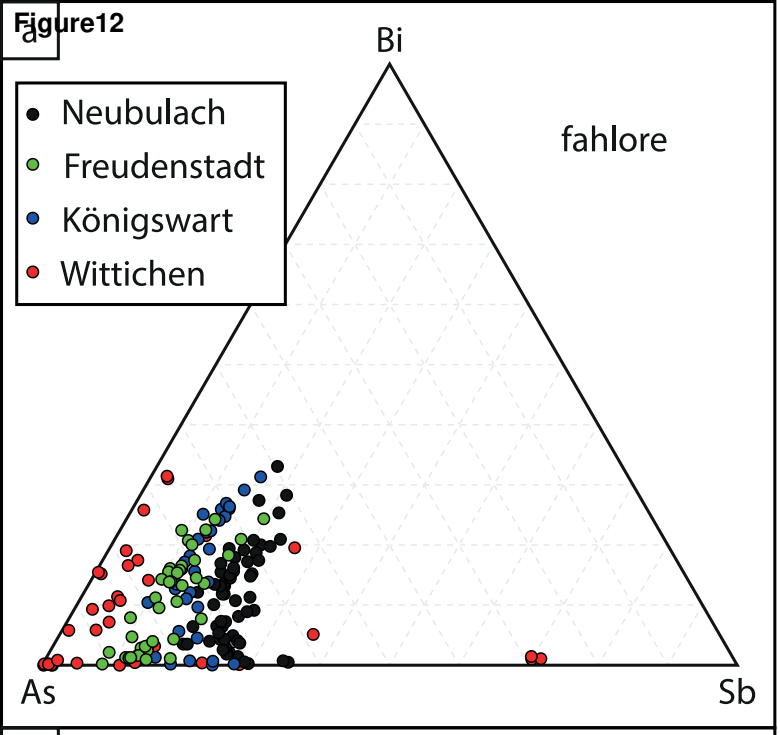
a
Bi
Neubulach
Freudenstadt
Königswart
Wittichen
fahlore
As
Sb

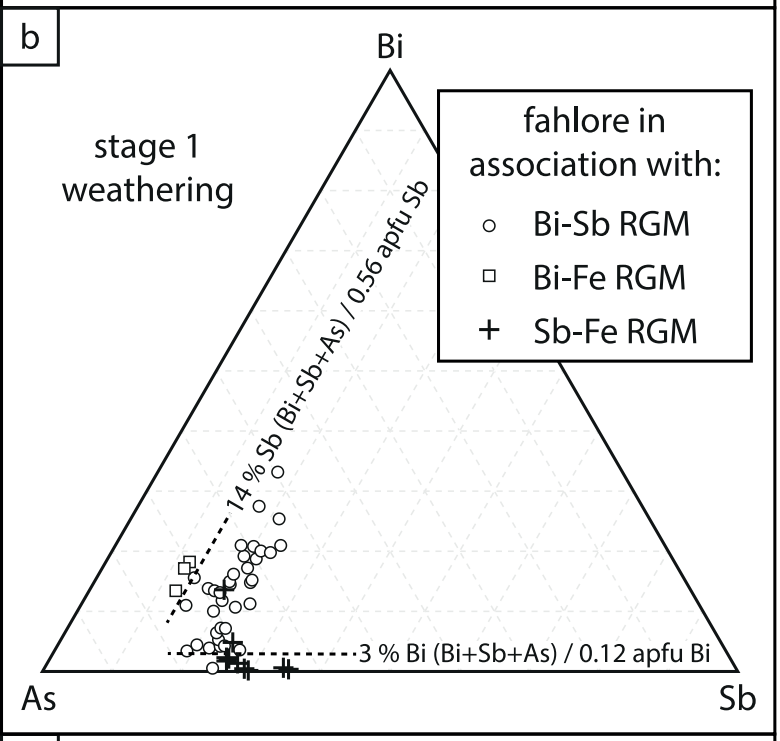
b
Bi
stage 1
weathering
fahlore in
association with:
Bi-Sb RGM
Bi-Fe RGM
Sb-Fe RGM
14 % Sb (Bi+Sb+As) / 0.56 apfu Sb
3 % Bi (Bi+Sb+As) / 0.12 apfu Bi
As
Sb

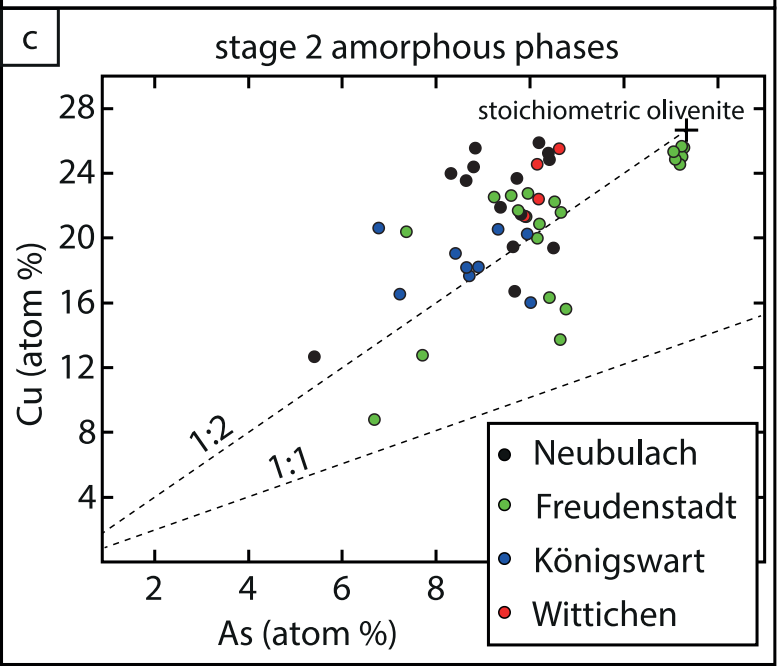
c
stage 2 amorphous phases
stoichiometric olivenite
28
24
20
16
12
8
4
Cu (atom %)
1:2
1:1
2
4
6
8
As (atom %)
Neubulach
Freudenstadt
Königswart
Wittichen

Figure 3

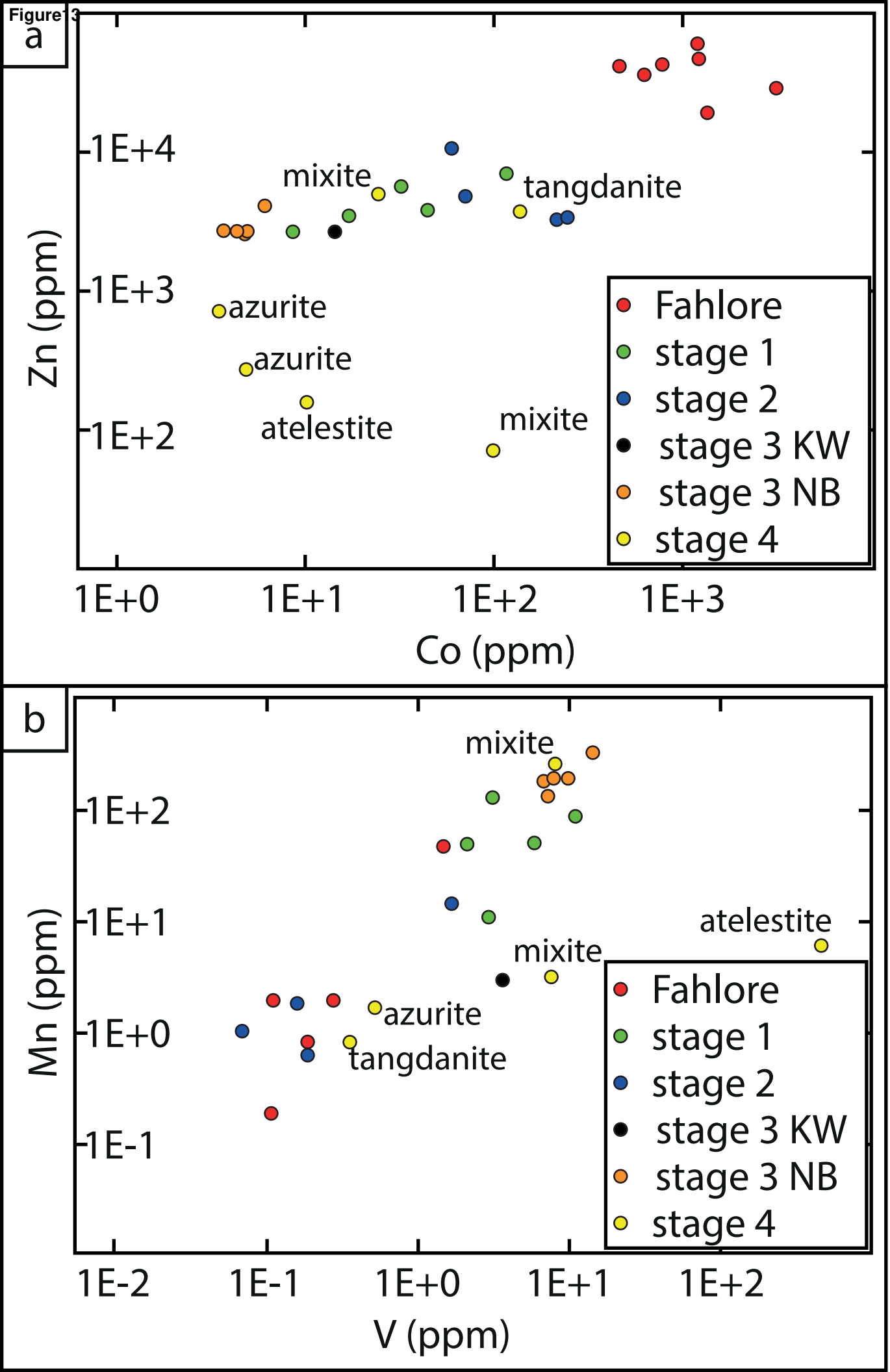
a
1E+4
1E+3
1E+2
Zn (ppm)
mixite
tangdanite
azurite
azurite
atelestite
mixite
Fahlore
stage 1
stage 2
stage 3 KW
stage 3 NB
stage 4
1E+0
1E+1
1E+2
1E+3
Co (ppm)
b
mixite
1E+2
1E+1
1E+0
1E-1
Mn (ppm)
atelestite
mixite
azurite
tangdanite
Fahlore
stage 1
stage 2
stage 3 KW
stage 3 NB
stage 4
1E-2
1E-1
1E+0
1E+1
1E+2
V (ppm)

Figure14

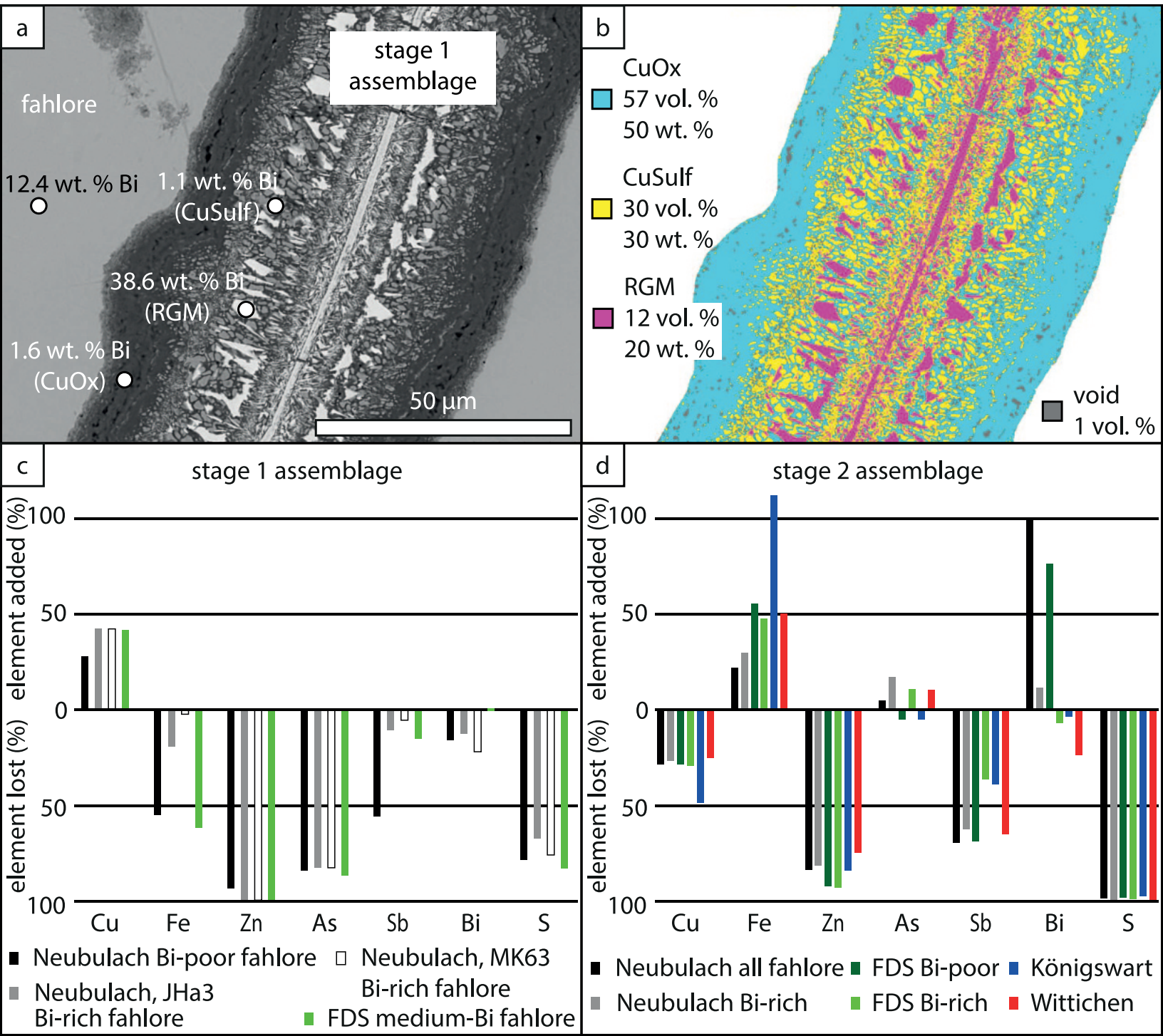
a
stage 1
assemblage
fahlore
12.4 wt. % Bi
1.1 wt. % Bi
(CuSulf)
38.6 wt. % Bi
(RGM)
1.6 wt. % Bi
(CuOx)
50 µm
b
CuOx
57 vol. %
50 wt. %
CuSulf
30 vol. %
30 wt. %
RGM
12 vol. %
20 wt. %
void
1 vol. %
c
stage 1 assemblage
element added (%)
element lost (%)
100
50
0
50
100
Cu
Fe
Zn
As
Sb
Bi
S
Neubulach Bi-poor fahlore
Neubulach, MK63
Bi-rich fahlore
Neubulach, JHa3
Bi-rich fahlore
FDS medium-Bi fahlore
d
stage 2 assemblage
element added (%)
element lost (%)
100
50
0
50
100
Cu
Fe
Zn
As
Sb
Bi
S
Neubulach all fahlore
FDS Bi-poor
Königswart
Neubulach Bi-rich
FDS Bi-rich
Wittichen

Figure15

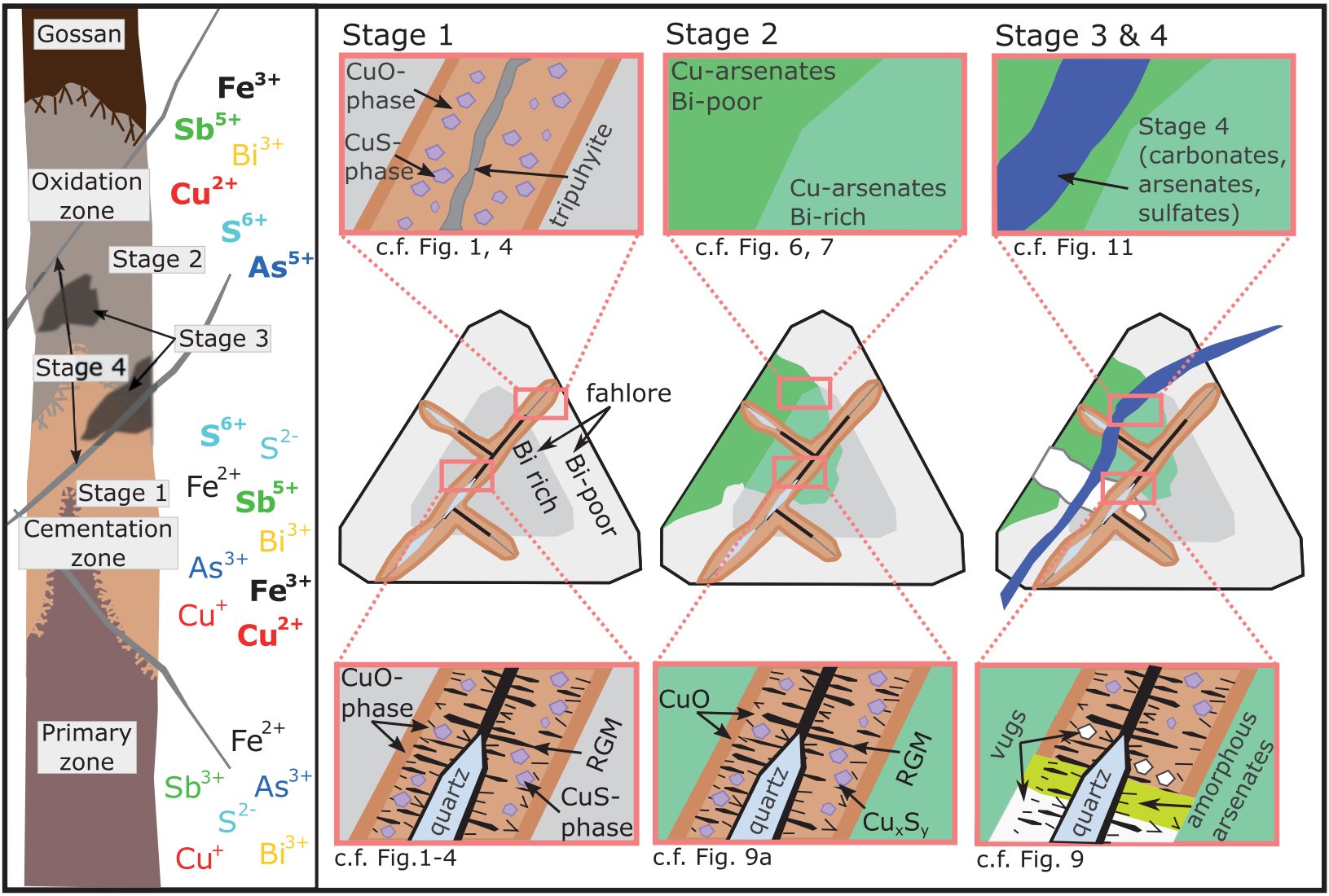
Gossan
Oxidation zone
Stage 2
Stage 3
Stage 4
Stage 1
Cementation zone
Primary zone
Fe3+
Sb5+
Bi3+
Cu2+
S6+
As5+
S2-
Fe2+
As3+
Cu+
Stage 1
Stage 2
Stage 3 & 4
CuO-phase
CuS-phase
tripuhyite
c.f. Fig. 1, 4
Cu-arsenates Bi-poor
Cu-arsenates Bi-rich
c.f. Fig. 6, 7
Stage 4 (carbonates, arsenates, sulfates)
c.f. Fig. 11
fahlore
Bi rich
Bi-poor
quartz
RGM
CuO
CuxSy
vugs
amorphous arsenates
c.f. Fig.1-4
c.f. Fig. 9a
c.f. Fig. 9

Electronic Annex Tables

Click here to download Electronic Annex: Tabellen ESM.docx

Electronic Annex Figure1

Click here to download Electronic Annex: supplementary Fig 1.eps

Electronic Annex Figure2

Click here to download Electronic Annex: supplementary Fig 2.eps

Electronic Annex Figure3

Click here to download Electronic Annex: supplementary Fig 3.eps

Electronic Annex Figure4

Click here to download Electronic Annex: supplementary Fig 4.eps

Electronic Annex Figure5

Click here to download Electronic Annex: supplementary Fig 5.eps

Electronic Annex Figure6

Click here to download Electronic Annex: supplementary Fig 6.eps